Contents lists available at ScienceDirect

Transactions of Nonferrous Metals Society of China

36(2026) 43−67

www.tnmsc.cn

Influence of minor Sc on microstructure and properties of AA7085 alloy

Ting-bin LIANG [a,#], Hong WANG [a,#], Jia-hai LI [a], Zhi-chao YANG [a], Bin WANG [a], De-yu ZHANG [a], Xiang-yi ZHANG [a], Asad ALI [b], Xi-zhou KAI [c], Yu-tao ZHAO [c], Shuang-bao WANG [a,d,*]

[a] Key Laboratory of LCR Materials and Devices of Yunnan Province, School of Materials and Energy, Yunnan University, Kunming 650091, China;
[b] Division of Energy Science, Luleå University of Technology, Luleå 97187, Sweden;
[c] School of Materials Science and Engineering, Jiangsu University, Zhenjiang 212013, China;
[d] Electron Microscopy Center, Yunnan University, Kunming 650091, China

---

Abstract: The age-hardening response, mechanical, and corrosion-resistant properties of AA7085 alloys with and without the addition of 0.3 wt.% scandium (Sc) were compared. Using advanced techniques such as aberration-corrected transmission electron microscopy and first-principles calculations, the underlying micromechanisms of Sc microalloying were revealed. Results show that the increase in strength of the AA7085-Sc alloy is mainly attributed to the decreased Al grain size and increased number density of both $Al_3Sc@Al_3(Sc,Zr)$ core−shell nanoparticles and Sc-containing η_p and GP−η_p nanoprecipitates. Strong strain fields and evident electron transfer from Zr to the neighboring matrix Al atoms exist at the $Al_3Sc@Al_3(Sc,Zr)/Al$ interface. The Sc doping in GP−η_p and η_p suppresses the GP−$\eta_p \rightarrow \eta_p$ transformation. Modified corrosion resistance of the AA7085-Sc alloy compared with AA7085 alloy is associated with the fine grain boundary precipitates of η phases and narrow precipitation free zone. The reasons of property changes of AA7085 alloy after Sc microalloying are explored based on the multiscale microstructural characterization.

Keywords: 7085 aluminum alloy; Sc microalloying; microstructure; property; transmission electron microscopy

---

1 Introduction

The 7000 series Al−Zn−Mg−Cu alloys, such as 7085 alloys investigated in the present study, are crucial light-weight structural materials in the aerospace industry (e.g. for aircraft stringers) since they offer a good combination of strength, damage tolerance and corrosion resistance [1]. Their properties mainly result from the contributions of microstructures at different scales, such as Al grain configuration and precipitate types [2−4]. It has been demonstrated that microalloying based on some unique elements like rare-earth Sc has a strong influence on the microstructures and thus is an important method to modulate the alloys' properties [5−8]. For the microalloyed multicomponent alloys, it is a vital requirement to understand the interaction between different microstructures and microalloying elements, and how these modified microstructures correlate with the resulting macroscopic properties from both experimental and theoretical viewpoints.

Characteristic microstructures of the wrought Al−Zn−Mg−Cu(−Zr) alloys are composed of Al grains decorated with high density second-phase particles. The equiaxed recrystallized Al grains distributed along the deformation direction are formed by solid solution at 420−475 °C for 0.5−2 h [8−11]. Their typical diameters are below 200 μm. Among the secondary-phase particles, the large

---

[#] Ting-bin LIANG and Hong WANG contributed equally to this work

Corresponding author: *Shuang-bao WANG, Tel: +86-13669721892, E-mail: sbwang0617@ynu.edu.cn

https://doi.org/10.1016/S1003-6326(25)66948-2
Received 10 April 2024; accepted 17 December 2024

constituent (primary) particles (e.g. $AlCr_2$ [12], *S*-Al_2CuMg [10,13], Al_3Zr [10], η-$MgZn_2$ [11,14] and Mg_4Zn_7 [15]) in the shape of short rod and irregular geometry are characterized by a size of 0.5−4 μm. These constituent particles are formed by a liquid−solid eutectic reaction and maintained after homogenization, deformation and solid solution. Formation of the Al_3Zr constituent particles promotes the heterogeneity and grain refinement of the 7000 series Al alloys during casting. The nanosized Al_3Zr phases are precipitated from Al grain interior and grain boundaries during homogenization treatment (~470 °C, 24 h), impeding the grain coarsening of the deformed 7000 series alloys during solid solution treatment [9]. The other fine-scale η-series precipitates with disc-like shapes are identified to be homogeneously distributed in the Al matrix with an average size below 7 nm [8,16,17]. They precipitate from the Al matrix at large extent during aging treatment at ~120 °C. Precipitation strengthening is the most important method among the various strengthening techniques for 7000 series Al alloys [18].

It is widely accepted that the age precipitation sequence that occurred in Al−Zn−Mg−Cu alloys can be expressed as supersaturated solid solution (SSSS) → Guinier−Preston (GP) zones → η' → η [19,20]. For GP zones, GP I zones are recognized as solute-rich clusters and GP II zones are featured with Zn-rich layers lying on $\{111\}_{Al}$. The η' precipitates ($Mg_2Zn_{5-x}Al_{2+x}$ with $x>0$ [16,21], or $Mg_4Zn_{13}Al_2$ [22]) that have the same habit plane as GPII zones are related to the peak hardness of the alloys. They are coherent with Al bulk on the broad interfaces and semi-coherent on the periphery interfaces. Equilibrium η phase ($MgZn_2$) is usually formed at an over-aging stage [14]. By atomic-scale transmission electron microscopy (TEM), two more precise precipitation processes were proposed to be (1) SSSS→GP−η_p → η_p → η and (2) SSSS → GP−η' → η' → η, where 7 atomic-layer-thick GP−η_p zones featured by structurally stable double atomic-panel and 11 atomic-layer-thick η_p-precipitates with metastable composition of $MgZn_4Al$ were determined [16,18]. In the second precipitation process, the early-stage GP−η' zones were described as the “cloudy” clusters with a variable thickness and without clear features. As one variant of η and destination phase of η', the plate-shape η_2 possesses the orientation with Al bulk of $[10\bar{1}0]_{\eta2}//[110]_{Al}$, $(0001)_{\eta2}//(1\bar{1}1)_{Al}$ [8,23]. It has a sandwich structure when viewed along $[110]_{Al}$ and a zigzag structure along $[1\bar{1}2]_{Al}$ zone axis. Rod-shape η_1 (another variant of η) has the orientation of $[1\bar{2}10]_{\eta1}//[110]_{Al}$, $(10\bar{1}0)_{\eta1}//(00\bar{1})_{Al}$ or $[0001]_{\eta1}//[110]_{Al}$, $(10\bar{1}0)_{\eta1}//(001)_{Al}$.

Extensive research indicates that the sole addition of Sc mainly induces the formation of Al_3Sc particles during casting and subsequent thermo-mechanical process, improving the properties of Al alloys by Al grain refinement and secondary-phase strengthening [24,25]. In 7085 alloy containing Zr, the addition of microalloying element Sc modifies specific strength, corrosion resistance, fatigue property and thermal stability [26−28]. Researchers focus on the structural characteristics of $Al_3(Sc,Zr)$ precipitates formed during thermal aging and their effects on the Al grain size and corresponding alloy properties. However, the factors how Sc influences the stability and interfacial structure of $Al_3(Sc,Zr)$/Al matrix have not been figured out and need further investigation. For example, related studies suggest that the coaddition of Zr and Sc causes the transformation of primary Al_3Sc into $Al_3(Sc,Zr)$, thereby elevating recrystallization temperature and refining Al grains by pinning effect [26,29,30]. In addition to the primary Al_3Sc particles, spherical $Al_3(Sc_{1-x}Zr_x)$ core-shell precipitates, with a Zr-enriched shell and an Sc-enriched core can be formed under high-temperature aging conditions (300−450 °C) [6,31]. The significantly slower diffusivity of Zr in Al compared to Sc helps stabilize the precipitates against coarsening to achieve high thermal stability up to ~300 °C [32]. Table 1 summarizes characteristics of the secondary-phase particles mentioned above based on previous well-established findings.

In contrast to the $Al_3(Sc,Zr)$ particles, there is limited atomic scale information, concerning the interaction between Sc and the η-series precipitates in Zr-containing Al−Zn−Mg−Cu alloys. SUN et al [35] pointed out that the corrosion-improved Al−Zn−Mg−Cu−Zr−Sc alloy has discontinuous but refined grain boundary precipitates (GBPs) due to the addition of Sc element. The study by PENG et al [9] suggested that the Sc addition leads to the formation of the *Y* phase and more η phases at the position 120 mm away from the quenching end in high-Zn-content Al−Zn−Mg−Cu−Sc alloys. TENG

Table 1 Characteristics of some related secondary-phase particles in 7000 series alloys

Second phase	Symmetry	Lattice parameter/Å	Phase type	Shape
$AlCr_2$ [12]	$P4/mmm$	a=b=3.00, c=8.64	Constituent particle	Irregular
S (Al_2CuMg) [10]	$Cmcm$	a=4.02, b=9.27, c=7.12	Constituent particle	Irregular
$Al_3(Sc,Zr)$ [10,33]	$I4/mmm$	a=b=4.01, c=17.28	Constituent particle	Irregular
			Dispersoid	Sphere
Mg_4Zn_7 [15]	$C2/m$	a=26.0, b=5.24, c=14.28	Constituent particle	Irregular
η/η_2 ($MgZn_2$) [8,14,23]	$P6_3/mmc$	a=b=5.15, c=8.48	Precipitate	Plate
η_1 ($MgZn_2$) [23]	$P6_3/mmc$	a=b=5.15, c=8.48	Precipitate	Rod
η' ($Mg_2Zn_{5-x}Al_{2+x}$) [21]	$P\bar{6}$	a=4.96, c=14.02	Precipitate	Disc
GP−η' (MgZn rich) [16]	Uncertain	Uncertain	Precipitate	Disc
η_p ($MgZn_4Al$) [16]	$P\bar{6}$	a=5.00, c=9.27	Precipitate	Disc
GP−η_p ($MgZn_{10}Al_9$) [18]	Uncertain	Uncertain	Precipitate	Disc
Y (Zn−Cu rich) [34]	$P6/mmm$	a=b=4.29, c=13.85	Precipitate	Plate

et al [36] reported that the Sc addition is in favor of the precipitation of the η' phase, but could also prevent the transformation of η' phase to η phase. LIU et al [29] observed that a higher content of Sc and Zr addition induces a higher density of precipitates with an excellent refinement effect. Nevertheless, the atomistic interplay between Sc and η-series precipitates has largely remained unexplored in prior studies.

Inspired by the above, the properties of the peak-aged 7085 alloy and 7085-Sc alloy were first compared on the basis of age-hardening monitoring, room-temperature tensile test, intergranular corrosion (IGC) and exfoliation corrosion (EFC) experiments. The atomically resolved high-angle annular dark-field (HAADF) and energy-dispersive X-ray spectroscopy (EDS) in scanning transmission electron microscopy (STEM), geometric phase analysis (GPA) and first-principles calculations were performed with the aim to reveal the micro-mechanisms of property changes induced by minor Sc addition. The achieved results are hoped to facilitate the design and development of high-performance Al−Zn−Mg−Cu alloys to meet the demands of specific aerospace applications.

2 Experimental

2.1 Alloys and heat treatment

Two different 7085 aluminum alloys with and without Sc microalloying were prepared under the same experimental conditions. The detailed chemical composition of the two alloys quantified by titrimetric analysis is given in Table 2.

Table 2 Composition of alloys studied (wt.%)

Sample	Zn	Mg	Cu	Zr	Sc	Cr	Si	Fe	Al
7085	8	1.2	2.2	0.15	−	0.06	0.06	0.1	Bal.
7085-Sc	8	1.2	2.2	0.15	0.3	0.06	0.06	0.1	Bal.

Several different master alloys and pure Al ingots were melted and cast into the cuboid iron mold. Before melting together with other alloying components, the Al−2wt.%Sc master alloy was first preheated to 640 °C for 1 h to ensure the complete dissolution of Sc into the molten aluminum. The alloy ingots after casting were air cooled to room temperature. They were then subjected to homogenization at 460 °C for 24 h, hot rolling at 420 °C in multiple passes with a 75% thickness reduction and cold rolling at room temperature in multiple passes with a 30% thickness reduction. The finally obtained 3 mm-thick plates were cut into small pieces of 10 mm × 10 mm × 3 mm by electric spark wire cutting for subsequent heat treatments. Solid solution (475 °C, 2 h) followed by rapid room-temperature water quenching and artificial aging in an oil bath of 120 °C for periods up to 192 h were sequentially applied to the small pieces of alloy samples.

2.2 Property tests

The Vickers hardness of the mechanically polished samples with different aging time was monitored by HVS−1000Z hardness tester (Shanghai Zhongyan Inc., China). The hardness value corresponding to each aging time of the sample was obtained by averaging 10 measurements. The peak-aged samples with dog-bone shape (2 mm in thickness and 25 mm in gauge length) were subjected to tensile testing at room temperature with a constant strain rate of 1 mm/min by an AGX-V Electronic Universal Tensile Testing Machine (Shimadzu Inc., Japan). The loading direction was along the rolling direction of the sample. At least three tensile samples for each group were tested to obtain an average tensile value.

For the intergranular corrosion (IGC) test, a corrosion solution was prepared with 57 g NaCl and 10 mL H_2O_2 per liter of distilled water according to ASTM G110—1992 standard evaluation criteria [37]. The sample surface area to volume of corrosion solution ratio was less than 20 mm^2/mL. The samples were soaked in the corrosion solution for 6 h at a constant temperature of (30±1) °C. After corrosion, the samples were taken out, washed with deionized water and then dried. The sides perpendicular to the broad surface were fixed with epoxy resin to prevent chamfering of the edges during polishing and then observed under an optical microscope. The exfoliation corrosion (EFC) was carried out according to GB/T 22639—2008 standard. The peak-aged samples were coated with epoxy resin and only the test surface was exposed to soak in corrosion solution of 4 mol/L NaCl + 0.5 mol/L KNO_3 + 0.1 mol/L HNO_3 at (25±1) °C. After 6 h and standard 48 h of corrosion, photographs were taken to assess the surface denudation grade of the samples.

2.3 Microstructural characterization

The STEM−HAADF observations were performed with a double aberration-corrected Spectra 300 X-FEG TEM (ThermoFisher Scientific, USA), which enables a spatial resolution of 60 pm under an acceleration voltage of 300 kV, a probe converged semi-angle of 18.6 mrad, and a collection angle range of 50−200 mrad. In atomic-scale HAADF image, it is easy to resolve different elements and their occupations in the structure due to the fact that the image contrast is known to be roughly proportional to the square of the atomic number, Z [38]. The Super-X G2 detection system installed on Spectra 300 TEM was used to characterize the element distribution in the region of interest. Independent determination of specimen thickness in the analysis region was conducted by electron energy loss spectroscopy (EELS) in STEM using a Continuum 1069 image filter (Gatan Inc., USA). To achieve true thickness, the sample relative thickness, t/λ, where t represents true thickness and λ represents the mean free path of inelastic loss, was first obtained from the analysis of the zero-loss peak of the EELS. Zero-loss peaks were collected under the following conditions: incident energy of 300 keV, convergence semi-angle of 0 mrad, camera length of 29 mm and collection semi-angle of 100 mrad under a spectrometer collection aperture of 5 mm. Samples for STEM measurements were prepared by mechanical punching, grinding, twin-jet electropolishing until perforation using Lebo TJ-100SE twin-jet electropolisher, and then plasma cleaning using a Gatan Solarus 955 advanced plasma cleaner. The electrolyte and temperature for twin-jet electropolishing are a solution of 25% HNO_3 + 75% CH_3OH and −25 °C, respectively.

The Al grain size of peak-aged samples was characterized by LM100 optical microscopy (Wright Optoelectronics, China) and symmetry electron backscattered diffraction (EBSD, Oxford company, UK). The mechanical polished and Keller's reagent etched sample surface was adopted for optical microscopy observation. The electro-polished surface of the unperforated STEM sample by twin-jet electropolishing was used for EBSD measurement. The phase identification of constituent particles in the peak-aged samples was carried out using a Rigaku SmartLab SE X-ray diffractometer (XRD) with Cu K_α radiation from 10° to 90° at a scan rate of 4 (°)/min. The sample surface electropolished for 10 s with a voltage of 20 V in an electrolyte of 25% HNO_3 + 75% CH_3OH at −25 °C was used for the phase analysis of XRD.

2.4 First-principles calculations

First-principles calculations were carried out using the CASTEP software package, which is based on density functional theory (DFT) with the generalized-gradient approximation (GGA)–Perdew-Burke-Ernzerhof (PBE) correlational function and ultra-soft pseudo potential USP plane wave [39]. The geometry optimization of the corresponding structures was done before the calculation of the energy. The convergence tests indicated that 280 eV was a sufficient cutoff for the ultrasoft pseudopotential to achieve high precision in the Al−Zn−Mg−Cu system. The formation enthalpies (ΔH) of the structures were defined and calculated. The formula used for ΔH calculations is as follows [40]:

$$\Delta H(\mathrm{Mg}_x\mathrm{Zn}_y\mathrm{Al}_z)=E(\mathrm{Mg}_x\mathrm{Zn}_y\mathrm{Al}_z)-x_{\mathrm{Mg}}E(\mathrm{Mg})-y_{\mathrm{Zn}}E(\mathrm{Zn})-z_{\mathrm{Al}}E(\mathrm{Al})$$

where $\Delta H(\mathrm{Mg}_x\mathrm{Zn}_y\mathrm{Al}_z)$ represents the enthalpy change of $\mathrm{Mg}_x\mathrm{Zn}_y\mathrm{Al}_z$, and $E(\mathrm{Mg}_x\mathrm{Zn}_y\mathrm{Al}_z)$ represents the total energy of each atom of $\mathrm{Mg}_x\mathrm{Zn}_y\mathrm{Al}_z$. The $x_{\mathrm{Mg}}=\dfrac{x}{x+y+z}$, $y_{\mathrm{Zn}}=\dfrac{y}{x+y+z}$ and $z_{\mathrm{Al}}=\dfrac{z}{x+y+z}$ are the fractions of Mg, Zn and Al in the $\mathrm{Mg}_x\mathrm{Zn}_y\mathrm{Al}_z$ structure, respectively. The $E(\mathrm{Mg})$, $E(\mathrm{Zn})$ and $E(\mathrm{Al})$ are the energies per atom in their equilibrium structures.

3 Results and discussion

3.1 Age hardening behavior and tensile property

Figure 1(a) shows the hardness vs aging time curves of the 7085 and 7085-Sc alloys at 120 °C, from which we can see the identical age-hardening behaviors of two different alloys. Specifically, both samples undergo a rapid age hardening from 0 to 5 h, a gradual hardness increase from 5 to 46 h and a slight hardness decrease from 46 to 70 h. Both samples present similar hardness plateaus with small hardness fluctuation after 70 h. The observed age-hardening behavior of the two samples is consistent with previous reports of similar alloys [8,18]. In comparison, the peak-aged hardness of the 7085-Sc alloy (HV 205.8) is higher than that of the 7085 alloy (HV 197.6). Additionally, 7085-Sc alloy always has higher hardness values than 7085 alloy in the over-aging stage, indicating better heat resistance of 7085-Sc alloy. As a result, one can conclude that the addition of 0.3 wt.% Sc has a positive effect on the age hardening of 7085 alloy.

The room-temperature tensile curves (Fig. 1(b)) and the corresponding extracted values (inset in Fig. 1(b)) of two peak-aged samples show that the 7085-Sc alloy has an ultimate strength (UTS) of 601.8 MPa and a yield strength (YS) of 548.8 MPa. The achieved strengths are higher than those of the 7085 alloy with UTS of 584.6 MPa and YS of 531.8 MPa. However, there is a decreased elongation (El) for 7085-Sc alloy (10.6%) as compared to the 7085 alloy (15.6%). Similarly, the increased strength and decreased elongation were also previously observed for the Sc-containing Al−Zn− Mg−Cu alloys relative to their counterparts without Sc addition [5,27]. On the contrary, both Sc-microalloyed 2000 series Al−Cu−Mg alloys and 6000 series Al−Mg−Si alloys present simultaneously improved strength and elongation [41,42]. The differentiated interaction between Sc and microstructure is expected to be the reason for the decreased elongation of 7085-Sc alloy. In short, the present results indicate that there are tremendous increases in hardness, strength and heat resistance but a decrease in elongation when the 0.3 wt.% Sc is added to the 7085 alloy.

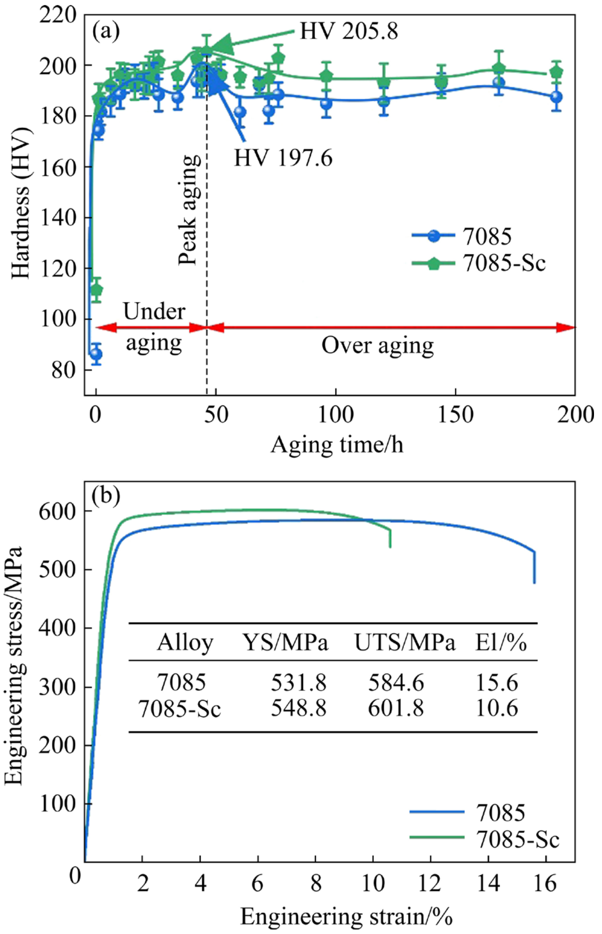

Alloy	YS/MPa	UTS/MPa	El/%
7085	531.8	584.6	15.6
7085-Sc	548.8	601.8	10.6

Fig. 1 Age-hardening behaviors of 7085 and 7085-Sc alloys at 120 °C (a) and room-temperature tensile curves of two peak-aged alloys (b)

3.2 Corrosion resistance of peak-aged samples

The effect of Sc addition on the corrosion resistance of 7085 alloy was evaluated by IGC and EFC experiments, as shown in Fig. 2. The IGC of peak-aged 7085 and 7085-Sc alloys was first

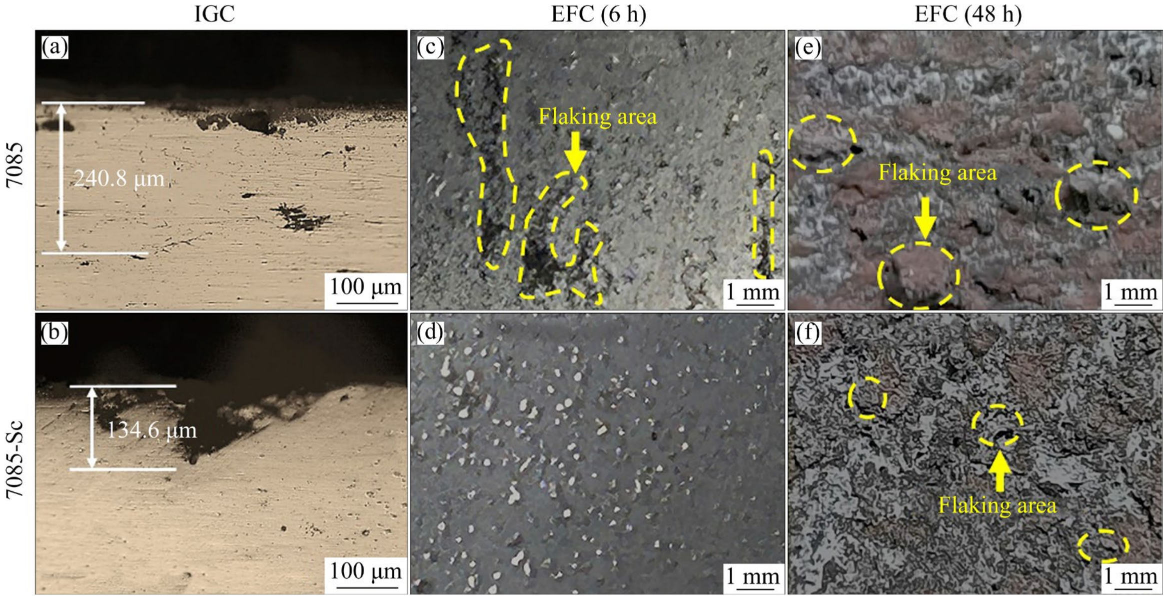

Fig. 2 Comparison of corrosion resistance of two peak-aged alloys: (a, b) Cross-sectional images showing IGC of 7085 and 7085-Sc alloys by optical microscopy; (c−f) Top-view images showing EFC of 7085 and 7085-Sc alloys after corrosion for 6 h and 48 h by photography, respectively

conducted by immersion corrosion test. The optical microscopy images of the corrosion cross section show that the 7085 alloy has a corrosion depth of 240.8 μm (Fig. 2(a)), while the 7085-Sc alloy exhibits a relatively smaller corrosion depth of 134.6 μm (Fig. 2(b)). Consequently, it can be concluded that the Sc microalloying contributes to the enhancement of IGC property of 7085 alloy. Similarly, the study by SHI et al [43] showed the 0.25Sc and 0.1Zr (wt.%) microalloying is in favour of the IGC property improvement of Al−5.4Zn−2.0Mg−0.35Cu (wt.%) alloys due to the larger spacing of GBPs [43]. Recently, SUN et al [35] also reported that sole 0.15 wt.% Sc addition to Al−7.0Zn−3.0Mg−0.3Cu−0.15Sc−0.12Zr (wt.%) alloy results in more excellent resistance to IGC. The discontinuous GBPs significantly reduce the anodic dissolution rate of the precipitates, thus increasing the resistance to IGC.

It is known that the EFC can significantly deteriorate the fatigue life of metals and alloys [44]. Normally, the EFC is induced by localized sub-surface (inter-granular in most cases) corrosion and subsequent grain lift-out, which leads to the formation of blisters on the surface of materials. Here, the samples undergoing a short 6 h and a standard 48 h of corrosion tests were monitored to better compare the EFC susceptibility. Figure 2(c) shows the corrosion morphology of 7085 alloy after 6 h of the EFC test. Notably, the dark and narrow contrast among the corrosion morphology of alloys indicates partial separation of metal (namely the blisters). It can be seen that there are some slight flaking areas (i.e. some areas encircled by yellow dashed lines) on the surface of 7085 alloy, indicating the onset of EFC. However, no flaking areas are detected on the surface of the 7085-Sc alloy after 6 h of EFC test (Fig. 2(d)), which means that the 7085-Sc alloy has an improved EFC property as compared to the 7085 alloy. A similar phenomenon is also observed for two different alloys after standard 48 h of EFC test, as shown in Figs. 2(e, f). As such, evident flaking areas occur on the surface of the 7085 alloy (Fig. 2(e)). In comparison, only a small number of tiny flaking areas are identified on the surface of the 7085-Sc alloy (Fig. 2(f)). The results of corrosion tests obtained for 7085-Sc alloy are significantly better than those of 7085 alloy. The microaddition of Sc simultaneously modifies the IGC and EFC properties of the 7085 alloy. Identical conclusions were obtained in a study where the EFC property of Al−Zn−Mg−Cu alloys can be improved by the additions of Sc and/or Zr due to the inhibition of recrystallization and larger spacing of grain boundary precipitates (GBPs) [43].

3.3 Grain size distribution of Al matrix of two different alloys

It is known that many properties of Al alloys are related to the shape and size of Al matrix grains. Here, the well-known EBSD along with metallographic microscopy were employed to determine the effect of minor addition of Sc on the configuration of Al grains in the 7085 alloy. Both EBSD image (Fig. 3(a)) and metallographic micrograph (Fig. 3(b)) show that the peak-aged 7085 alloy is composed of equiaxed and elongated grains, indicating full recovery and recrystallization of Al grains after solid solution treatment. Statistical analysis shows that the 7085 alloy possesses an average Al grain size of ~32 μm (Fig. 3(c)). Figures 3(d−f) present the configuration of Al grains in the peak-aged 7085-Sc alloy. Similar to 7085 alloy, the 7085-Sc alloy also consists of a large number of equiaxed grains (Figs. 3(d, e)). Nevertheless, the size of Al grains is substantially decreased from ~32 to ~8 μm when 0.3 wt.% Sc is added to the 7085 alloy. Therefore, it can be concluded that the addition of Sc has a notable refining effect on the grains of Al matrix, which is consistent with previous published works [9,27,28].

Hall−Petch equation, $\sigma_{\mathrm{gb}}=kd^{-1/2}$ (k represents a scaling constant), indicates that there is an inverse relationship between the yield strength (σ_{gb}) and the grain size (d). The calculation result shows that grain refinement-induced yield strength increment of 7085-Sc alloy is 12 MPa relative to 7085 alloy when k is taken as 68 MPa/μm$^{-1/2}$ [11]. The tensile test shows that the yield strength of 7085-Sc alloy is at least 17 MPa higher than that of the 7085 alloy (inset in Fig. 1(b)). Therefore, it cannot deny that Sc-induced Al grain refinement of 7085-Sc alloy is mainly responsible for the increased yield strength of 7085-Sc alloy. Different from the Al grain size of Sc-containing 2000 series Al−Cu−Mg alloys (exceeding 15 μm) [42] and 6000 series Al−Zn−Mg−Cu alloys (exceeding 51 μm) [7,41], the quite small Al grain size of 8 μm makes the yield strength to ultimate strength ratio of 7085-Sc alloy is close to 1 (~0.91 for the present study), contributing to the degraded elongation despite of the increased strength of 7085-Sc alloy (Fig. 1(b)). In the case of corrosion property, the corrosion paths through the fine grain surface layer are, as expected, longer than those for the coarse-grained surface layer. The longer the corrosion path

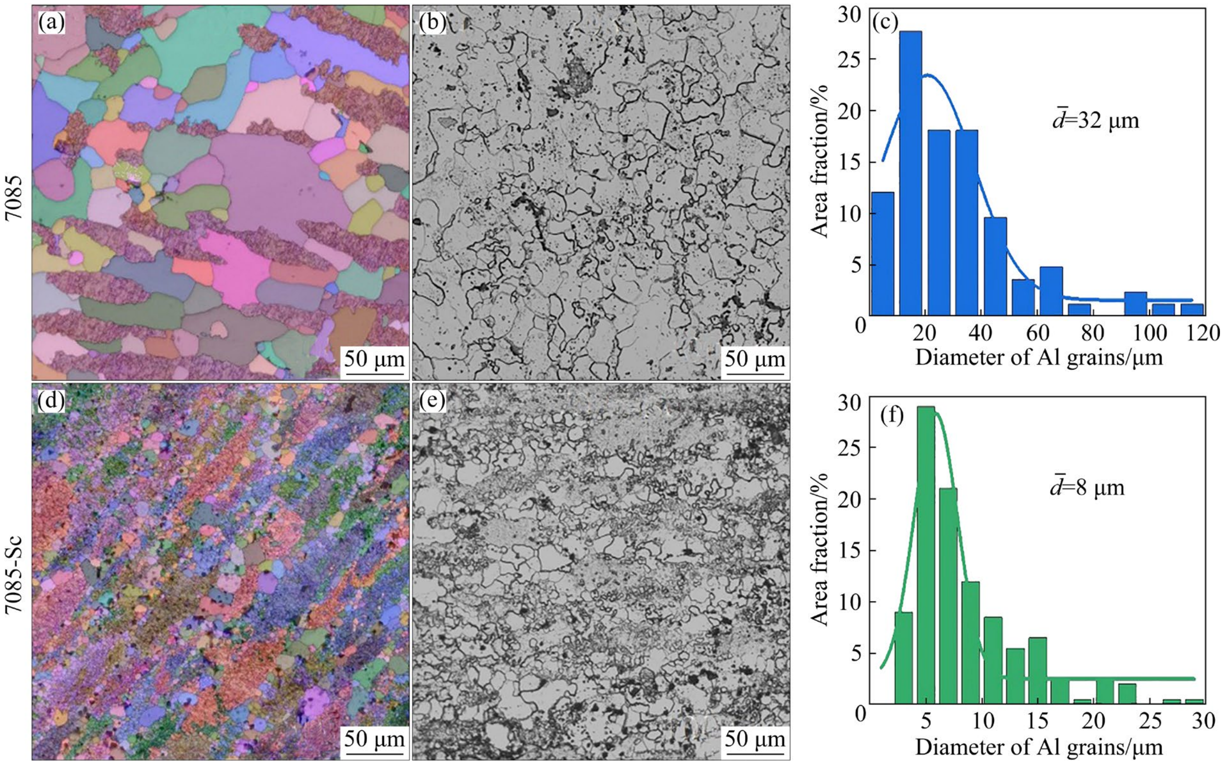

Fig. 3 Morphology and size distribution of Al grains in peak-aged 7085 and 7085-Sc alloys: (a, b, d, e) Typical EBSD images (all Euler angle maps) and metallographic images, respectively, showing consistent configurations of Al grains for two different characterization methods in same alloys; (c, f) Statistical grain size distribution

at a given corrosion depth, the better the intergranular corrosion resistance exhibited by the Al alloy. As a result, the enhanced IGC of 7085-Sc alloy is attributed to the refinement of Al grains, which serve as physical barriers that slow down the spread of IGC [42].

3.4 Coarse second-phase particles in two different alloys

It is particularly well-suited for XRD to determine the incoherent secondary-phase particles in metals and alloys. For this reason, the XRD was initially used to identify the coarse constituent phases in two peak-aged 7085 and 7085-Sc alloys, as shown in Fig. 4. Considering that the content of coarse constituent particles in the alloy samples is prevailingly less than 1 wt.%, the sample surfaces were first electropolished to expose more constituent particles on the analyzed surfaces before XRD analyses. Figure 4(a) shows that both alloys have sharp diffraction peaks corresponding to *α*(Al) phase. In addition, some very weak diffraction peaks are also visible except the sharp Al peaks. To identify these secondary phases associated with the weak peaks, the vertical coordinate of Fig. 4(a) was enlarged to clearly see the positions of the weak peaks, as shown in Fig. 4(b). Careful analysis indicates that some Al_3Zr, Mg_4Zn_7, $AlCr_2$ and Al_2CuMg phases can be found in the 7085 alloy.

In comparison, the 7085-Sc alloy also comprises the Al_3Zr, Mg_4Zn_7, $AlCr_2$ and *S*-Al_2CuMg phases. However, an additional $Al_3(Sc,Zr)$ phase that is characterized by the peaks at 26.5° and other multiphase overlapping peaks at 20.3°, 37.3° and 40.2° appears in the 7085-Sc alloy. It is worth noting that the unique peaks at 41.9°, 43.7° and 81.3° confirm the existence of the Al_3Zr in the 7085-Sc alloy though some overlapping peaks are found for the Al_3Zr and $Al_3(Sc,Zr)$ phases. Besides, the peaks at 78.5° shown in the insets of Fig. 4(a) highlight the existence of the $AlCr_2$ phase in the 7085 and 7085-Sc alloys in addition to its overlapping peaks. The Sc addition leads to the extra formation of primary $Al_3(Sc,Zr)$ phases in addition to the Al_3Zr. These primary particles promote the heterogeneity and grain refinement of the 7085-Sc alloys during casting. This partly explains the smaller Al grain size of 7085-Sc alloy than that of 7085 alloy shown in Fig. 3. Herein, it is still difficult to imagine the shape, size and distribution of the coarse constituents in the two alloys based on the XRD analyses. In view of this, more intuitive STEM−HAADF and STEM−EDS analyses were employed to characterize the configurations of these coarse constituent particles in the 7085 and 7085-Sc alloys.

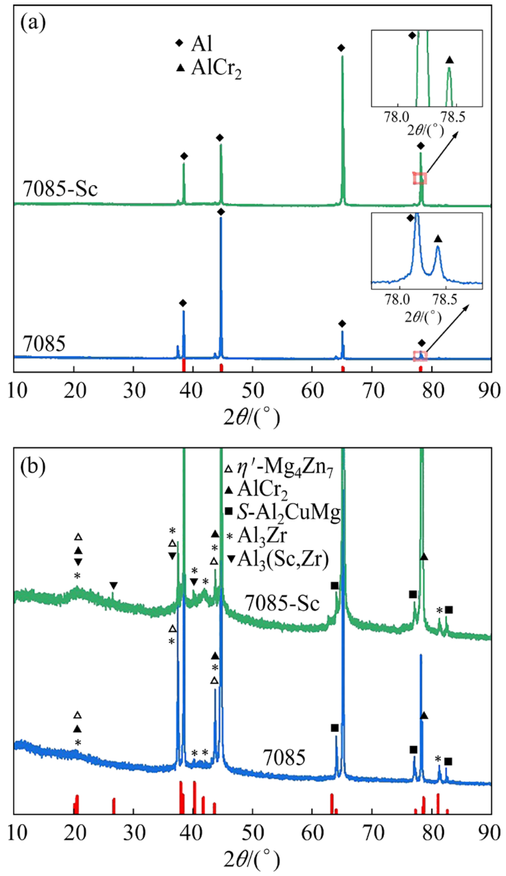

Fig. 4 XRD patterns revealing main phase compositions in peak-aged 7085 and 7085-Sc alloys: (a) XRD overview showing strong peaks of Al matrix and some weak peaks of secondary-phase particles; (b) Partial spectra of (a) with magnified peak intensity showing compositions of coarse constituent phases in alloys

Figures 5(a, c) show considerable irregular secondary-phase particles in two different peak-aged alloy samples. Close observation reveals that some coarse constituent particles of about 200 nm in size can be located both inside Al grains (such as those indicated by green arrows) and at grain boundaries (such as those indicated by red arrows) for two different alloys. The statistical measurements show that the 7085-Sc alloy has a decreased size distribution (100−200 nm) of coarse constituent particles as compared to that of 7085 alloy (100−300 nm), as shown in Figs. 5(b, d). As a consequence, microalloying Sc to 7085 alloy induces overall reduced size of constituent particles.

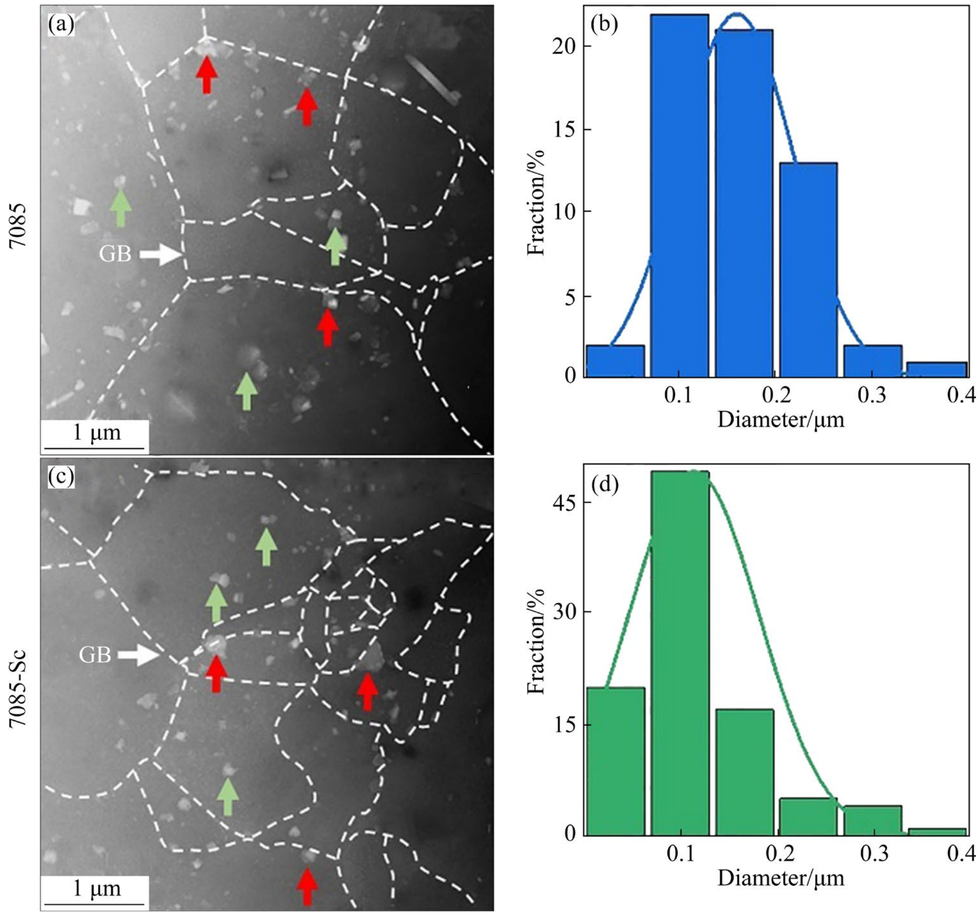

Fig. 5 Morphology and size distribution of coarse constituent particles in peak-aged 7085 and 7085-Sc alloys: (a, c) Low-magnification STEM−HAADF images; (b, d) Corresponding size distribution

STEM−EDS mapping results (Fig. 6) show that the different phases in two peak-aged alloy samples are in good agreement with the XRD results shown in Fig. 4. At grain boundaries of the 7085 alloy, some large particles with size exceeding 100 nm are usually identified to be composite particles such as $Mg_4Zn_7/AlCr_2$, $Mg_4Zn_7/AlCr_2/S$ and Mg_4Zn_7/Al_3Zr in addition to the individual $AlCr_2$ and Al_3Zr particles, as shown in Figs. 6(a−h). Melting points of the constituent particles are in the order of Al_3Zr > Al_3Sc > $AlCr_2$ > α(Al) > S > Mg_4Zn_7 phases. The Al_3Zr and $AlCr_2$ particles are first formed in the molten liquid. There is a probability for $AlCr_2$ to form in contact with Al_3Zr, generating $Al_3Zr/AlCr_2$ composite particles. After the molten liquid was solidified below 528.3 °C, the S and Mg_4Zn_7 particles start to form from α(Al) sequentially during the cooling process. A proportion of S and Mg_4Zn_7 particles are prone to nucleate and grow at the Al_3Zr and/or $AlCr_2$, thereby forming various composite particles due to favorable heterogeneous nucleation. These (composite) particles with substantially reduced particle size are retained when subjected to homogenization, hot rolling, cold rolling and solid solution. Some fine Al_3Zr particles with size below 50 nm shown in Fig. 6(a) mainly result from high-temperature homogenization treatment [9].

Compared to the 7085 alloy, primary $Al_3(Sc,Zr)$ constituent particles instead of Al_3Zr are observed at grain boundaries of the 7085-Sc alloy, as shown in Figs. 6(i−p). Their morphology and size are roughly consistent with those of Al_3Zr particles observed in the 7085 alloy. Similar to the 7085 alloy, the large composite particles of $Al_3(Sc,Zr)/Mg_4Zn_7/AlCr_2/S$ are also identified at grain boundaries of the 7085-Sc alloy. Some particles with interior bright and dark contrast (such as those particles pointed by the green arrow in Fig. 5(c)) also confirm the existence of identical composite particles inside the Al grains of 7085-Sc alloy. In addition, fine individual particles with a size less than 50 nm are identified to be $Al_3(Sc,Zr)$ and Mg_4Zn_7. The Sc microalloying of the 7085 alloy mainly contributes to the formation of $Al_3(Sc,Zr)$ and the decreased size distribution of

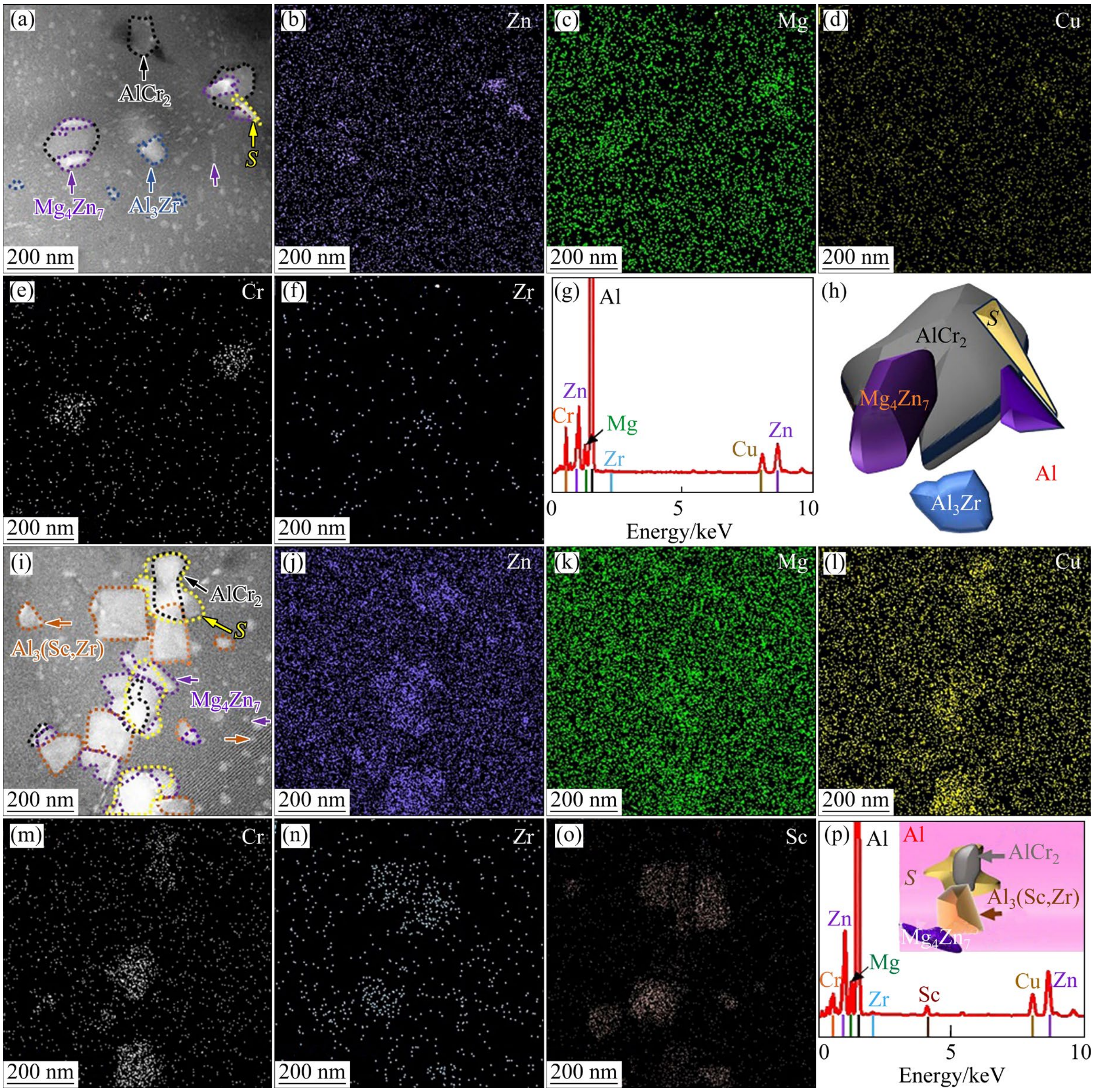

Fig. 6 STEM−HAADF and STEM−EDS results showing configurations of coarse constituent particles in two peak-aged alloys: (a−h) High-magnification HAADF image, corresponding elemental mappings, EDS spectrum and three-dimensional (3D) schematic illustration of particles in 7085 alloy; (i−p) High-magnification HAADF image, corresponding elemental mappings, EDS spectrum with 3D schematic illustration of particles (inset) in 7085-Sc alloy

coarse constituent particles in the 7085-Sc alloy. The smaller grain size of 7085-Sc alloy shown in Fig. 3(f) could be attributed to the presence of heat-resistant $Al_3(Sc,Zr)$ particles in the alloy.

The effect of a minor Sc addition on the spherical Al_3Zr nanoprecipitates in the peak-aged 7085 alloy was investigated by STEM−HAADF imaging and STEM−EDS analyses. Figure 7(a) shows a large number of Al_3Zr nanoparticles uniformly distributed in the Al matrix of peak-aged 7085 alloy. The average diameter of these nanoparticles is measured to be around 28 nm. Figure 7(b) shows an atomic-resolution HAADF image of one Al_3Zr used for STEM−EDS analysis. Figures 7(c, d) present elemental mappings of the Al and Zr from area of (b), respectively, where apparent elements Al and Zr are seen at the position of Al_3Zr particle. Line scanning analysis (Fig. 7(e)) along the line in (b) and EDS spectrum acquired from (b) show a high concentration of Zr in the particle, demonstrating that the observed nanoparticles belong to Al_3Zr. Figure 7(g) gives a schematic illustration of Al_3Zr particle with a spherical shape and uniform composition based on observed result.

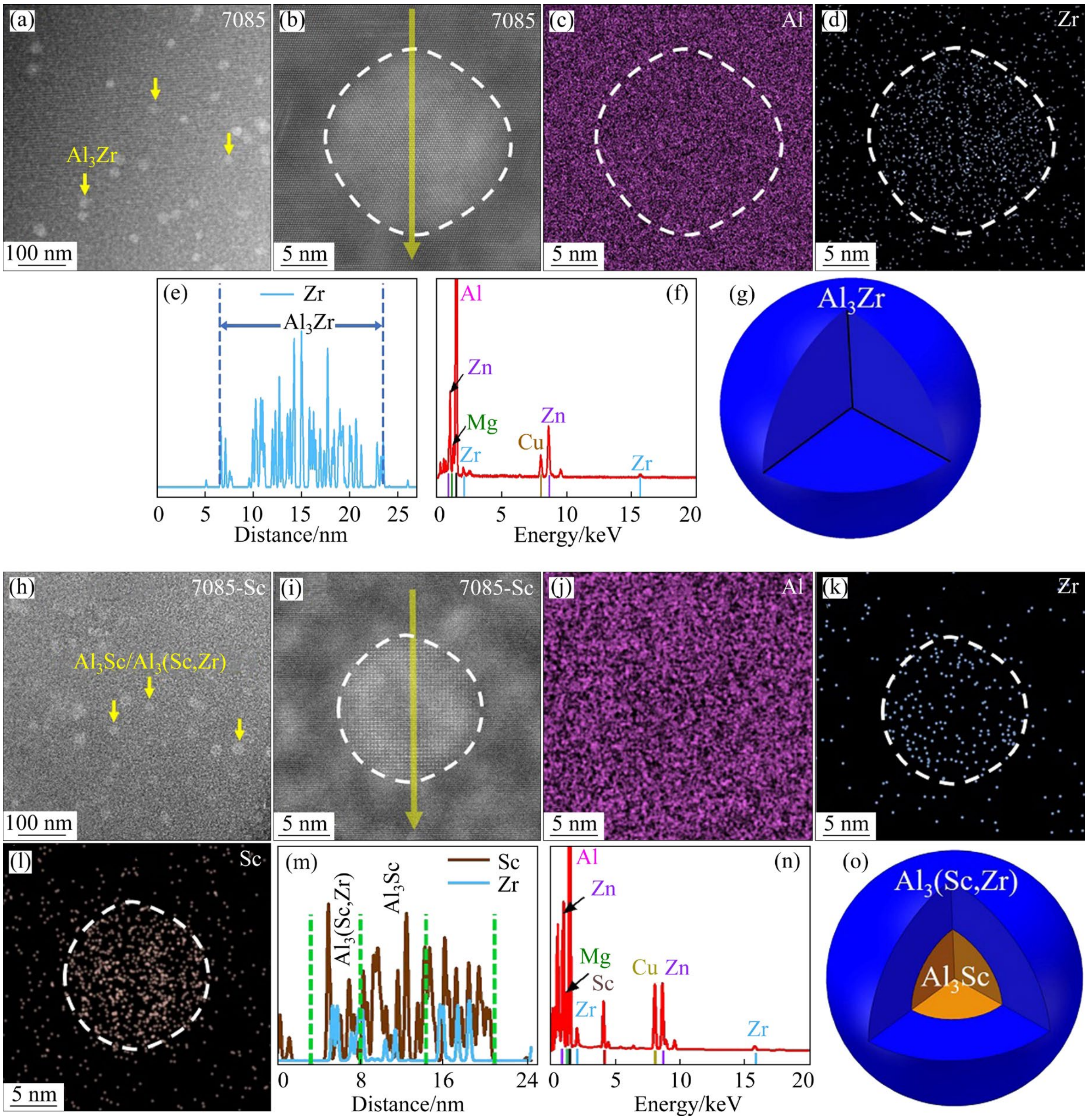

Fig. 7 Change of spherical Al_3Zr dispersoids in two peak-aged alloys: (a) Low-magnification HAADF image of Al_3Zr in 7085; (b) Atomic-resolution HAADF image of Al_3Zr in 7085; (c, d) Corresponding EDS mappings of Al and Zr in (b), respectively; (e) Concentration line profiles scanned along yellow arrow in (b); (f) EDS spectrum of Al_3Zr in (b); (g) Sectional illustration of Al_3Zr; (h) Low-magnification HAADF image of $Al_3(Sc,Zr)$ in 7085-Sc; (i) Atomic-resolution HAADF image of $Al_3(Sc,Zr)$ in 7085-Sc; (j−l) Corresponding EDS mappings of Al, Zr and Sc in (i), respectively; (m) Concentration line profiles scanned along yellow arrow in (i); (n) EDS spectrum of $Al_3(Sc,Zr)$; (o) Sectional illustration of $Al_3(Sc,Zr)$

Figure 7(h) shows the low-magnification HAADF image in which a lot of spherical nanoparticles with bright contrast are observed in the peak-aged 7085-Sc alloy. The average diameter of these nanoparticles is around 18 nm, which is smaller than that in 7085. Compared to Fig. 7(a), it can be observed that these spheres are more evenly distributed and present in greater numbers. Having a closer look at Fig. 7(h), some dark areas appear inside the particles, which is different from the uniform contrast of Al_3Zr particles in Fig. 7(a). Figure 7(i) shows an atomic-resolution HAADF image of one typical nanoparticle used for EDS analysis, in which the shell appears brighter than the core. Since Zr has a larger atomic number than Sc (40Zr and 21Sc), the bright shell corresponds to a Zr-enriched part of the precipitates. The EDS elemental mappings show that the particle is composed of Al, Zr and Sc, as shown in Figs. 7(j−l), respectively. Concentration profiles (Fig. 7(m)) along the line in (i) and EDS spectrum (Fig. 7(n)) from the area in (i) indicate that the core of the particle is mainly rich in Sc. Meanwhile, the Zr concentration increases at the periphery of the particle, thus forming a core−shell nanoparticle of $Al_3Sc@Al_3(Sc,Zr)$, as schematically shown in Fig. 7(o).

The decomposition of a supersaturated solid solution of Sc,Zr-containing Al alloys generates precipitation of the Al_3Sc, Al_3Zr and $Al_3(Sc,Zr)$ phases. The precipitation temperature of the $Al_3(Sc,Zr)$ and Al_3Zr nanoparticles is generally higher than 300 °C [33,45] and thus these particles are very thermally stable during high-temperature exposure. Studying the precipitation kinetics of $Al_3(Sc,Zr)$ phase, LEFEBVRE et al [46] found that the diffusion rate of Sc in Al matrix is higher than that of Zr under the same thermodynamic conditions. Therefore, the introduction of Sc in 7085 alloy leads to the preferential nucleation of Al_3Sc nanoparticles during aging. After that, the core−shell structure of $Al_3Sc@Al_3(Sc,Zr)$ is formed by the simultaneous segregation of Sc and Zr at the primary Al_3Sc. There is a robust precipitation of the $Al_3Sc@ Al_3(Sc,Zr)$ nanoparticles in the 7085-Sc alloys since the Al_3Sc serves as an excellent heterogeneous nucleating agent for the precipitation of $Al_3(Sc,Zr)$. A much higher density of $Al_3Sc@Al_3(Sc,Zr)$ nanoparticles can effectively impede the movement of dislocations and grain boundaries, thereby effectively refining grain structure (Fig. 3) and improving the thermal stability (Fig. 1(a)) of 7085-Sc alloy.

GPA analyses were conducted to figure out the strength-related interfacial Al strain field induced by Al_3Zr and $Al_3Sc@Al_3(Sc,Zr)$ nanoprecipitates, as shown in Fig. 8. A high-resolution HAADF image (Fig. 8(a)) shows an exemplified Al_3Zr particle surrounded by Al matrix in the peak-aged 7085 alloy. The corresponding EDS elemental mappings (Figs. 8(b−d)) of Al, Zr and Sc confirm that the observed Al_3Zr particle is free of Sc. GPA result, i.e. ε_{xx}, ε_{yy}, ε_{xy} and R_{xy}, of the corresponding HAADF image reveals weak lattice distortion at the interfacial Al matrix (Figs. 8(e−h)), implying a very small interfacial Al strain field induced by Al_3Zr particle (such as the site pointed by the yellow arrow in Fig. 8(f)). It is worth noting that similar interfacial Al strain field results were also achieved by GPA analyses of at least five Al_3Zr particles. This might mean a stress-release interface between Al_3Zr and Al matrix.

Figure 8(i) presents high-resolution HAADF image involving a typical $Al_3Sc@Al_3(Sc,Zr)$ nanoprecipitate and surrounding Al matrix in the peak-aged 7085-Sc alloy. Its corresponding EDS elemental mappings (Figs. 8(j−l)) confirm that the observed nanoparticle contains Sc in addition to Al and Zr. Figures 8(m−p) show the GPA result of ε_{xx}, ε_{yy}, ε_{xy} and R_{xy} of Fig. 8(i). Different from the Al_3Zr particle, extensive observation indicates that the $Al_3Sc@Al_3(Sc,Zr)$ nanoprecipitates cause strong lattice distortion (e.g. ≥5%) at the surrounding Al matrix, such as those sites pointed by yellow arrows in Figs. 8(m, o, p). The nucleation and growth of $Al_3(Sc,Zr)$ around the Al_3Sc increase the total interface mismatch strain energy. It is difficult for $Al_3Sc@Al_3(Sc,Zr)$ particle to mediate interfacial strain in time due to the slow growth. This way is not applicable to the relatively rapid growth of Al_3Zr by reducing the large surface energy. The finding of the present study well illustrates another reason for the higher strength of 7085-Sc alloy than 7085 alloy in the light of the strong interfacial strain field between $Al_3Sc@Al_3(Sc,Zr)$ and Al matrix.

The first-principles calculations have been performed to account for the stability of Al_3Sc with Zr segregation (namely the formed shell structure of $Al_3(Sc,Zr)$) during the thermal exposure. The segregation behavior of Zr at Al_3Sc/Al interface is assessed in terms of formation enthalpy (ΔH) of Al_3Sc/Al supercells with different percentages of Sc replaced with Zr, as shown in Fig. 9. It is seen that the Al_3Sc/Al supercell has a negative ΔH of −34.1 kJ/mol per atom. There is a gradual decrease in ΔH as Sc substitution in Al_3Sc by Zr increases. It is found that the $Al_3(Sc_{0.2},Zr_{0.8})$/Al structure has the lowest ΔH of −38.2 kJ/mol per atom among different supercell models. After full substitution of Sc by Zr, slightly increased ΔH (−37.0 kJ/mol per atom) is obtained for Al_3Zr/Al supercell. The present results indicate that the Zr segregation to Al_3Sc embedded in Al matrix is an energetically favored process, which is in agreement with the results from the three dimensional atom probe (3DAP) analysis [6]. In addition, it is difficult to obtain a pure Al_3Zr shell outside of the Al_3Sc core as a result of its increased ΔH.

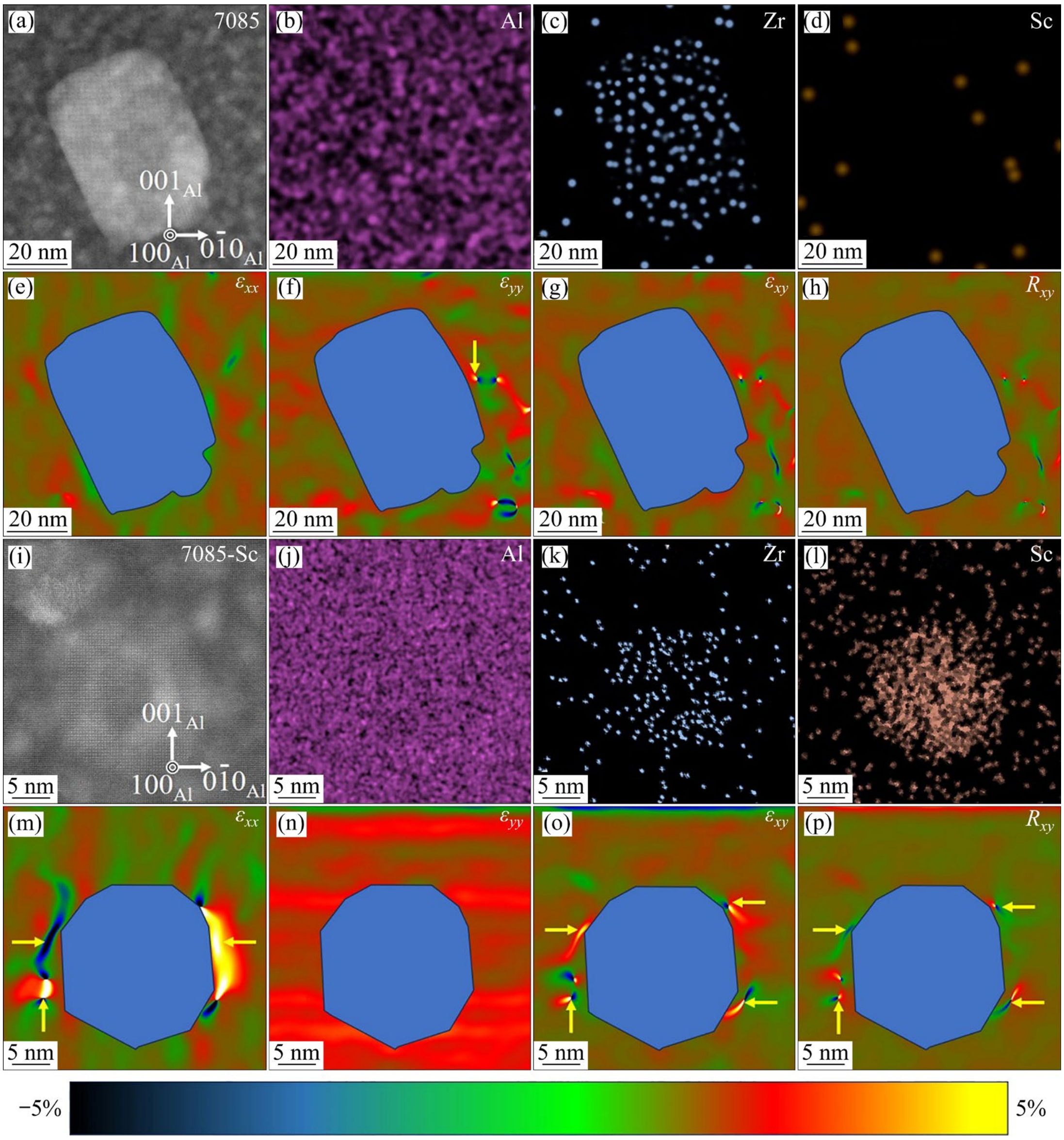

Fig. 8 GPA results of Al_3Zr precipitates in peak-aged 7085 alloy and $Al_3Sc/Al_3(Sc,Zr)$ precipitates in peak-aged 7085-Sc alloy: (a) High-resolution HAADF image of Al_3Zr precipitate in 7085 alloy; (b−d) Corresponding EDS elemental mappings of Al, Zr and Sc, respectively; (e−h) Corresponding matrix lattice distortion ε_{xx}, ε_{yy}, ε_{xy} (corresponding to shear) and R_{xy} (corresponding to lattice rotation) around precipitate, respectively; (i) High-resolution HAADF image of $Al_3Sc/Al_3(Sc,Zr)$ precipitate in 7085-Sc alloy; (j−l) Corresponding EDS elemental mappings of Al, Zr and Sc, respectively; (m−p) Corresponding matrix lattice distortion ε_{xx}, ε_{yy}, ε_{xy} and R_{xy} around precipitate, respectively

Figure 10(a) shows apparent $Al_3Sc@Al_3(Sc,Zr)$ precipitate in the 7085-Sc alloy. Figure 10(b) shows some evident interfacial Al strain field of ε_{yy} around the precipitate, which is in line with the result of Figs. 8(m, o, p). To clearly identify the interfacial mismatch dislocations, the high-resolution HAADF image of Fig. 10(b) was first fast-Fourier-transformed to obtain corresponding reflection spots, as shown in Fig. 10(c). By selecting two symmetric reflection spots of $(001)_{Al}$ and $(00\bar{1})_{Al}$ with small circles, applying mask and inversing FFT, an IFFT image was obtained, as shown in Fig. 10(d). Figures 10(e, f) show two enlarged interfacial structures (corresponding to two yellow dashed square areas in Fig. 10(d)) between $Al_3(Sc,Zr)$ shell and Al matrix. Close inspection at the interfaces reveals some edge dislocations at the strong strain field areas. In addition, it is noted that the extra atomic planes of the edge dislocations are at the side of the Al matrix. Here, the lattice mismatch between

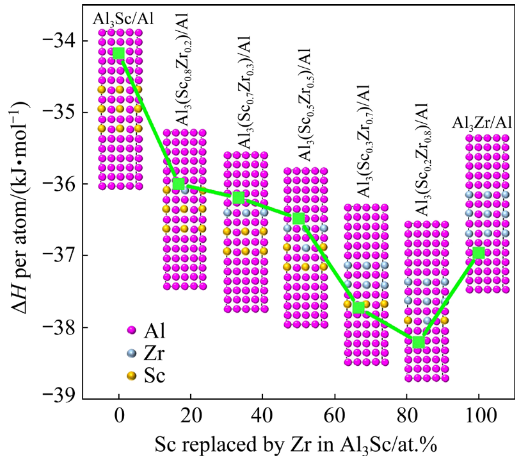

Fig. 9 Variation of ΔH with different percentages of Sc in Al_3Sc replaced with Zr embedded in Al matrix

different $Al_3(Sc,Zr)$ phases and the surrounding Al matrix is also illustrated by the first-principles structural relaxation of different supercell structures (Fig. 10(g)). The result shows a 0.48% lattice mismatch between Al_3Sc and surrounding Al matrix, which implies lager lattice parameter of Al_3Sc than Al matrix. The lattice mismatch turns to be −0.52% when 20% Sc in Al_3Sc is substituted by Zr, meaning that the lattice parameter of $Al_3(Sc_{0.2},Zr_{0.8})$ is smaller than that of the surrounding Al matrix. The Sc substitution in $Al_3(Sc_{0.8},Zr_{0.2})$/Al supercell by Zr is found to increase the lattice mismatch, and the lattice mismatch is increased to around −1.66% with 50% and 70% Sc substitution by Zr. A study by KHARAKTEROVA et al [47] also presents 1.5%

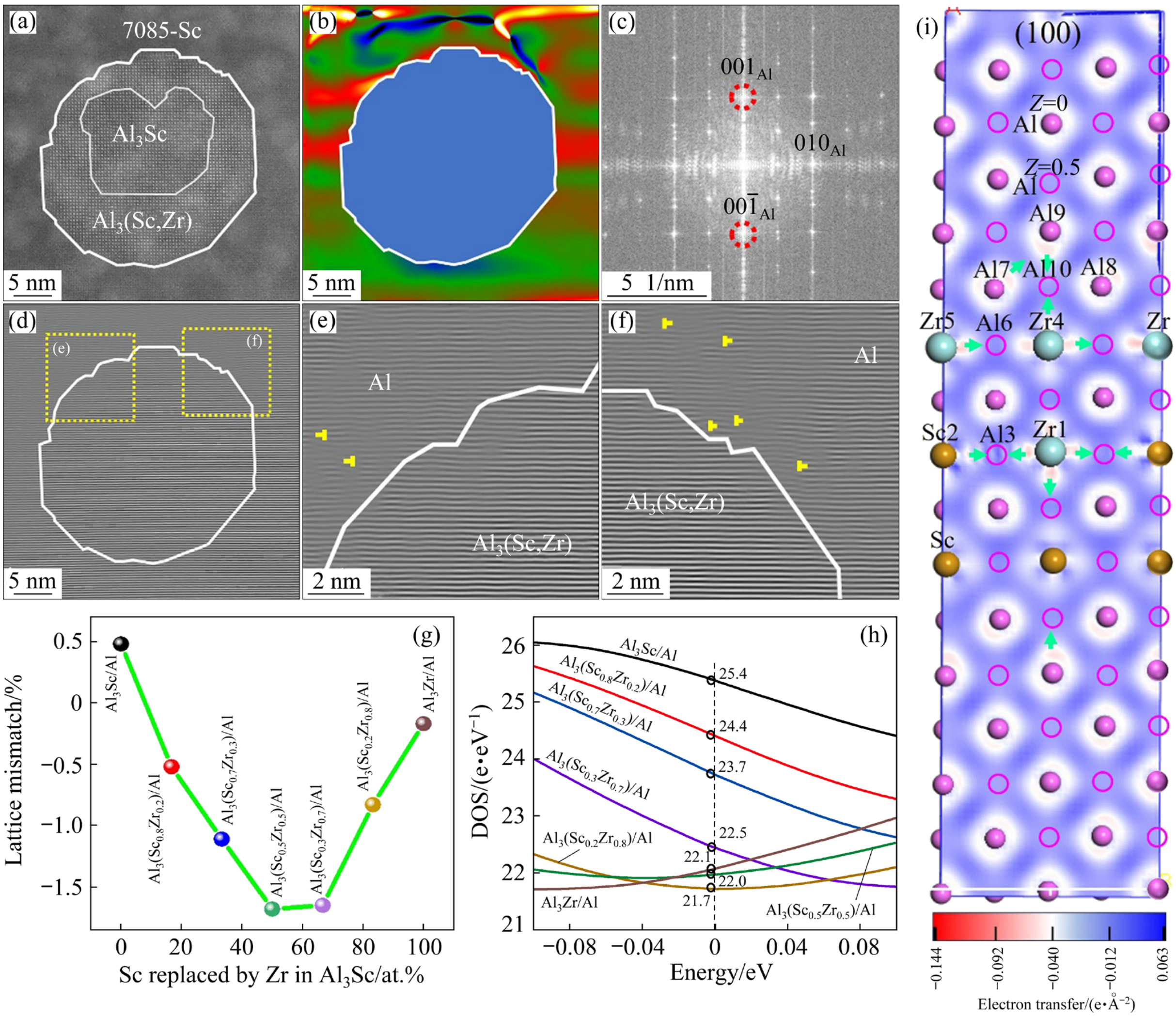

Fig. 10 Interfacial analyses between $Al_3(Sc_x,Zr_{1-x})$ (x=0−1) and Al matrix: (a−c) High-resolution HAADF image, corresponding strain field distribution of ε_{yy} obtained from GPA measurement and FFT, respectively; (d) Inverse FFT using reflection spots of $(001)_{Al}$ and $(00\bar{1})_{Al}$ in (c); (e, f) Magnified images from yellow dashed rectangle regions in (d) showing interfacial mismatch dislocations; (g) Variation of lattice mismatch between $Al_3(Sc_x,Zr_{1-x})$ and surrounding Al matrix after full relaxation; (h) Variation of DOS of different $Al_3(Sc_x,Zr_{1-x})$/Al structures; (i) Charge density difference 2D slice of exemplified $Al_3(Sc_{0.5},Zr_{0.5})$ structure at x−y atomic plane with z=0

mismatch between $Al_3(Sc,Zr)$ with Al matrix. However, there is an apparent decrease in the lattice mismatch when the substitution percentage of Zr in Al_3Sc exceeds 70%. The lattice mismatch is decreased to −0.17% for the Al_3Zr/Al supercell, indicating that the Zr segregation to Al_3Sc can reduce lattice parameters of Al_3Sc and induce large interfacial Al strain fields. The present results well explain the observed mismatch dislocations at the interface of $Al_3(Sc,Zr)$/Al, as shown in Figs. 10(e, f).

In addition, the DOS (Fig. 10(h)) and atomic bonding (Fig. 10(i)) in different structures are also simultaneously evaluated. As shown in Fig. 10(h), the $Al_3(Sc,Zr)$/Al configurations behave with basic metallic characteristics since their DOS near the Fermi level shows finite values [48]. In comparison, the Al_3Sc/Al configuration has the highest DOS of 25.4 e/eV near the Fermi level. As the substitution percentage of Sc in Al_3Sc/Al by Zr is increased from 0% to 50%, the DOS values at the Fermi level decrease gradually to 22.0 e/eV, implying decreased electrical conductivity. However, the DOS value slightly increases to 22.5 e/eV when the amount of Zr in the $Al_3(Sc,Zr)$ accounts for 70%. The DOS values again decrease to 21.7 e/eV and 22.1 e/eV for the $Al_3(Sc_{0.2},Zr_{0.8})$/Al and Al_3Zr/Al configurations, respectively, with further increased substitution percentage of Zr. In short, the Zr segregation to the superficial area of Al_3Sc induces the reduction of DOS values at the Fermi level, which is expected to result in a decrease in the electrical conductivity of alloy. Properties of Al−Zn−Mg−Cu alloys can be significantly altered by considering $Al_3(Sc,Zr)/Al_3Sc$ precipitates, and the current findings represent an important step forward in the characterization and exploration of these superficial $Al_3(Sc,Zr)$ shells at the nanometer scale.

The charge density difference was calculated to gain insights into the electron transfer among different atoms in an exemplified $Al_3(Sc_{0.5},Zr_{0.5})$/Al supercell, as shown in Fig. 10(i). As observed, both Zr1 and Sc2 atoms in the $Al_3(Sc_{0.5},Zr_{0.5})$ can transfer electrons to the nearest neighbor Al3 atom in between. Similarly, there is also obvious electron transfer from Zr4 and Zr5 atoms in $Al_3(Sc_{0.5},Zr_{0.5})$ to the nearest neighbor Al6 atom in between. In the case of the interface between $Al_3(Sc_{0.5},Zr_{0.5})$ and Al matrix, it is found that electron transfer occurs from Zr4 in the $Al_3(Sc_{0.5},Zr_{0.5})$ and Al9 in the Al matrix to interfacial Al10 in the middle. In addition, the electrons lost by Al7 and Al8 atoms also transfer to the nearest neighbor Al9 atom. The Hirshfeld analysis shows that the amount of lost electrons of each Zr atom (~0.050 e) is larger than that of each Sc atom (~0.037 e) in the supercell. In other words, Zr is easier to transfer electrons than Sc in the $Al_3(Sc_{0.5},Zr_{0.5})$/Al supercell to the neighboring Al atoms. It should be pointed out that the special Sc and Zr could lead to the formation of ionic bonding with the first and second nearest Al atoms at the Al/$Al_3(Sc,Zr)$ interface in addition to the basically metallic bonding. Such strong bonding is beneficial for inhibiting the coarsening of $Al_3Sc/Al_3(Sc,Zr)$ precipitates in the 7085-Sc alloy shown in Fig. 7 [49]. To the best of our knowledge, Sc-doped Al_3Zr exhibits increased lattice mismatch and decreased electric conductivity for the stable $Al_3(Sc_{0.2},Zr_{0.8})$/Al, which represents the novel findings in the field of alloy research.

In addition to the Al_3Zr phase, the influence of Sc microalloying on the age-hardening precipitates at 120 °C in 7085 alloy was also examined through HAADF imaging, EELS thickness measurement, EDS mapping analysis and first-principles calculations. Previous study has indicated that the $\langle 112\rangle_{Al}$ and $\langle 110\rangle_{Al}$ are two suitable observation directions to obtain the edge-on atomic structures of the disc-like strengthening precipitates in the Al−Zn−Mg−Cu alloy [16].

Figure 11(a) shows the high-density disc-like precipitates in the peak-aged 7085 alloys. Figure 11(b) shows a typical HAADF image of GP−η_p precipitates viewed along $\langle 112\rangle_{Al}$, which is characterized by a thickness of 7-atomic-layers in the $\{111\}_{Al}$ planes with two bright external double-panel structures and a relatively dark interior area. Figure 11(c) shows another typical HAADF image of η_p precipitates. in which at least 11 atomic-layer thickness in the $\{111\}_{Al}$ planes with bright ordered interior area is clearly resolved. There is no significant difference in the external double-panel structures between GP−η_p and η_p structures. In the early work [16], it was concluded that this double-panel structure, with the outermost layer composed of a mixture of Zn and Mg atoms and the inner layer consisting of two different positions of Zn, facilitates the formation of η_p. Similarly, peak-aged 7085-Sc alloy also exhibits high density GP−η_p and η_p precipitates in the Al matrix, as shown in Figs. 11(d−f). Figures 11(g, h) compare the diameter

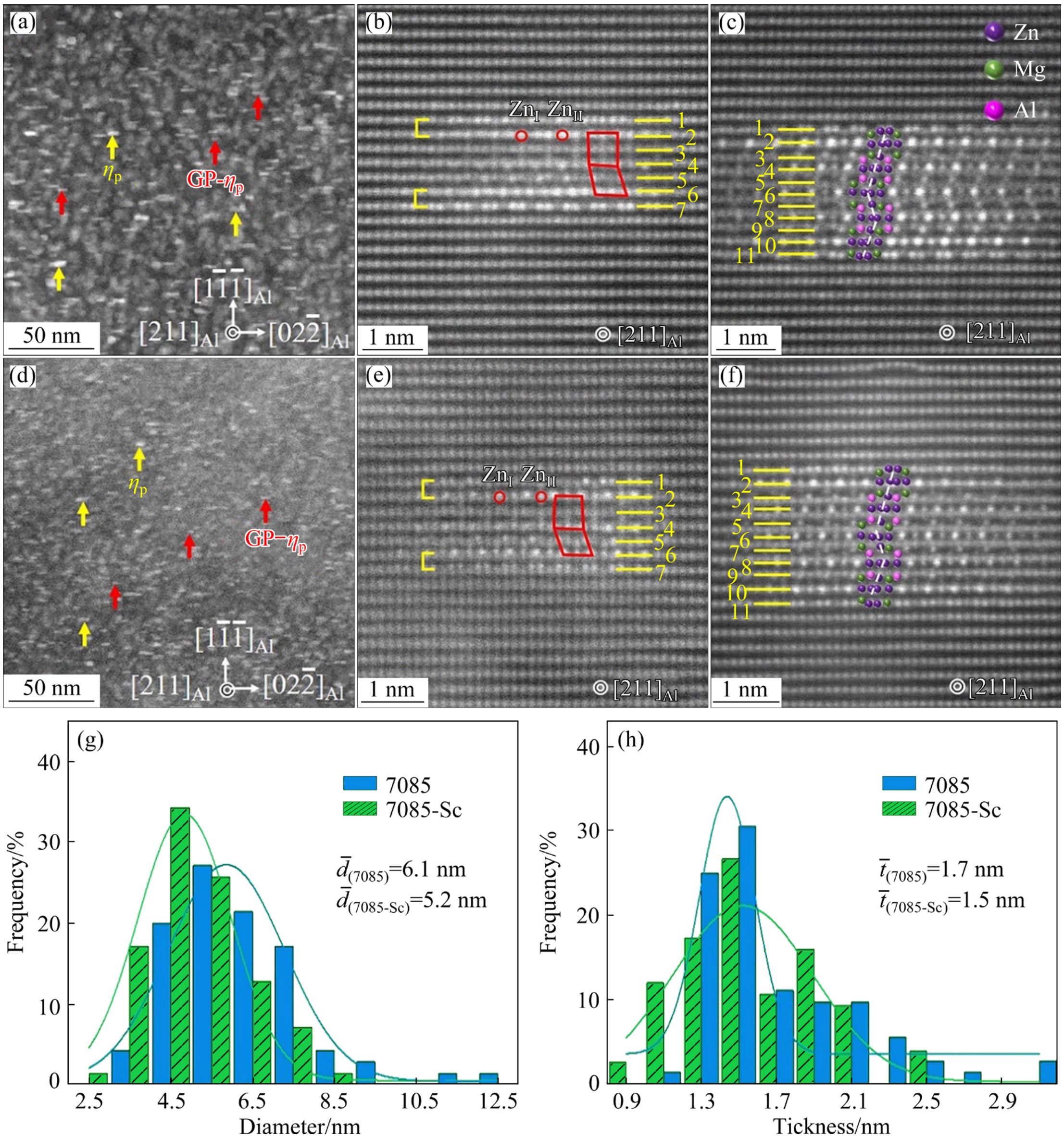

Fig. 11 Morphology, types and size distribution of nanoprecipitates in peak-aged (46 h, 120 °C) 7085 and 7085-Sc alloys: (a−c) HAADF images of precipitate microstructural overview, representative GP−η_p and η_p at atomic scale in 7085; (d−f) HAADF images of precipitate microstructural overview, atomic-scale GP−η_p and η_p in peak-aged 7085-Sc; (g, h) Comparison of average diameter ($\bar{d}$) and average thickness ($\bar{t}$) of disc-like precipitates in two alloys

and thickness of disc-like precipitates in the peak-aged 7085 and 7085-Sc alloys. The statistical results show that the precipitates in the 7085 alloy have an average diameter of 6.1 nm, which is larger than that (5.2 nm) of the 7085-Sc alloy. In addition, a smaller average thickness of precipitates (1.5 nm) is also identified in the 7085-Sc alloy as compared to 1.7 nm of the 7085 alloy. The above measurement indicates that addition of Sc to the 7085 alloy induces the refinement of peak-aging precipitates, implying a strong interaction between precipitates and Sc solutes.

Low-magnification high resolution HAADF images (Fig. 12) were further analyzed to check the influence of Sc addition on the proportion of the peak-aging GP−η_p and η_p precipitates in two peak-aged alloys. Previous study has shown that the GP−η_p and η_p precipitates have an intrinsic thickness of 7 and 11 atomic-layers in the $\{111\}_{Al}$ layers, respectively [16]. In addition, the brighter interior area of η_p structure than that of GP−η_p structure in HAADF image can also be complementary criteria to discriminate them. Based on these criteria, the proportion of the GP−η_p and η_p precipitates can be

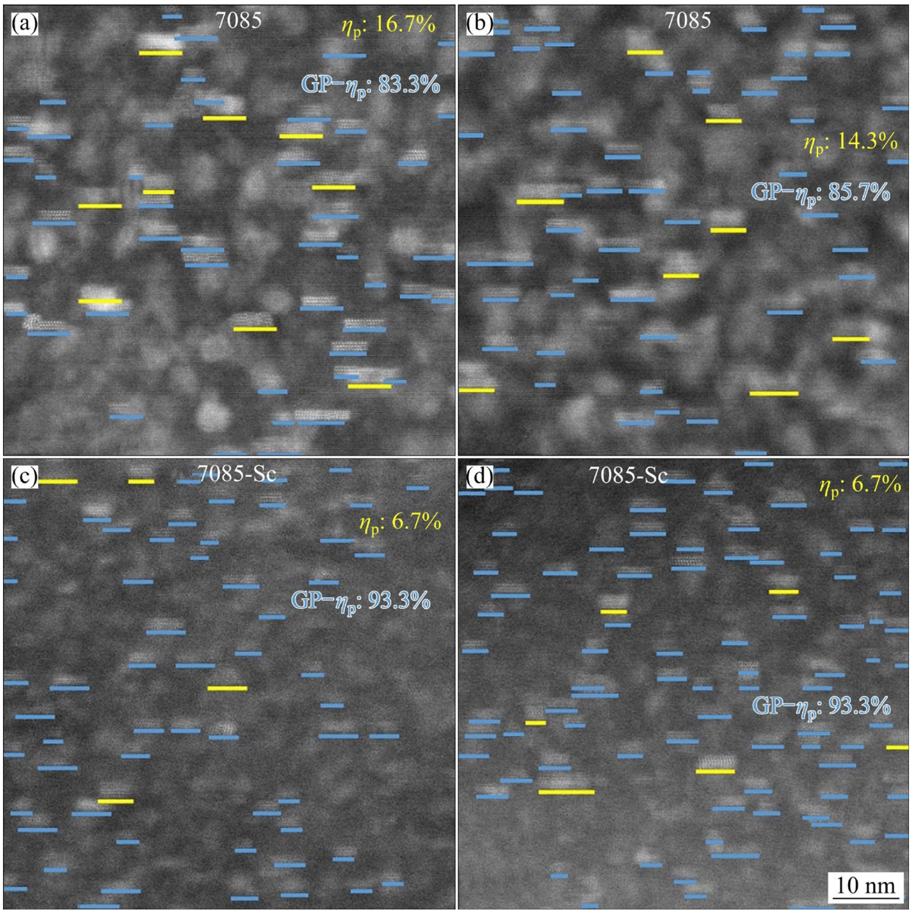

Fig. 12 Statistical results showing change of proportion of GP−η_p (marked by blue horizontal lines nearby) and η_p (marked by yellow horizontal lines nearby) precipitates in peak-aged 7085 and 7085-Sc alloys: (a, b) Two different observation areas used for analysis in 7085 alloy; (c, d) Two different observation areas used for analysis in 7085-Sc alloy

well measured using the low-magnification high-resolution HAADF images.

It is observed from Fig. 12 that the GP−η_p and η_p precipitates are the primary hardening particles in both peak-aged 7085 and 7085-Sc alloys. Consistently, LIU et al [18] also found that more than 90% of formed precipitates are the η_p-precipitates and the GP−η_p zones in the 7055 alloy with a high Zn content. In the peak-aged 7085 alloy (Figs. 12(a, b)), the relative proportions of the GP−η_p and η_p precipitates are 84.5% and 15.5%, respectively, in terms of statistical measurement. However, the relative proportions of GP−η_p and η_p precipitates become to be 93.3% and 6.7%, respectively, in the peak-aged 7085-Sc alloy (Figs. 12(c, d)). Thus, it is clear that the Sc addition has a visible suppression effect on the phase transformation from GP−η_p to η_p precipitates, leading to the increased proportion of GP−η_p in the peak-aged 7085-Sc alloy in comparison to the peak-aged 7085 alloy. A possible reason is that higher vacancy binding energy of Sc and Zr compared to the solute atoms (Zn, Mg and Cu) in the alloys [50] may suppress the diffusion of solute atoms through the vacancies, thus restricting the GP−η_p phase transformation and η_p formation.

The number of precipitates per volume (termed as number density of the precipitates in the context) is known to be critical information for the precipitation strengthening of Al alloys. To clarify this point, the STEM−EELS was further employed to characterize the thickness (t) of the observing area to obtain the number density of the precipitates. Figures 13(a, c) show two typical high-resolution HAADF images of the GP−η_p and η_p precipitates in the peak-aged 7085 and 7085-Sc alloys, respectively. Figure 13(b) shows the relative thickness (t/λ) of the sample at the positions P1, P2, P3 and P4 in Fig. 13(a). A Script Package of the Mean Free Path Estimator in EELSTools built into Gatan's Digital Micrograph gives a λ of ~100 nm for 300 keV electrons in Al matrix under an acceptance angle of

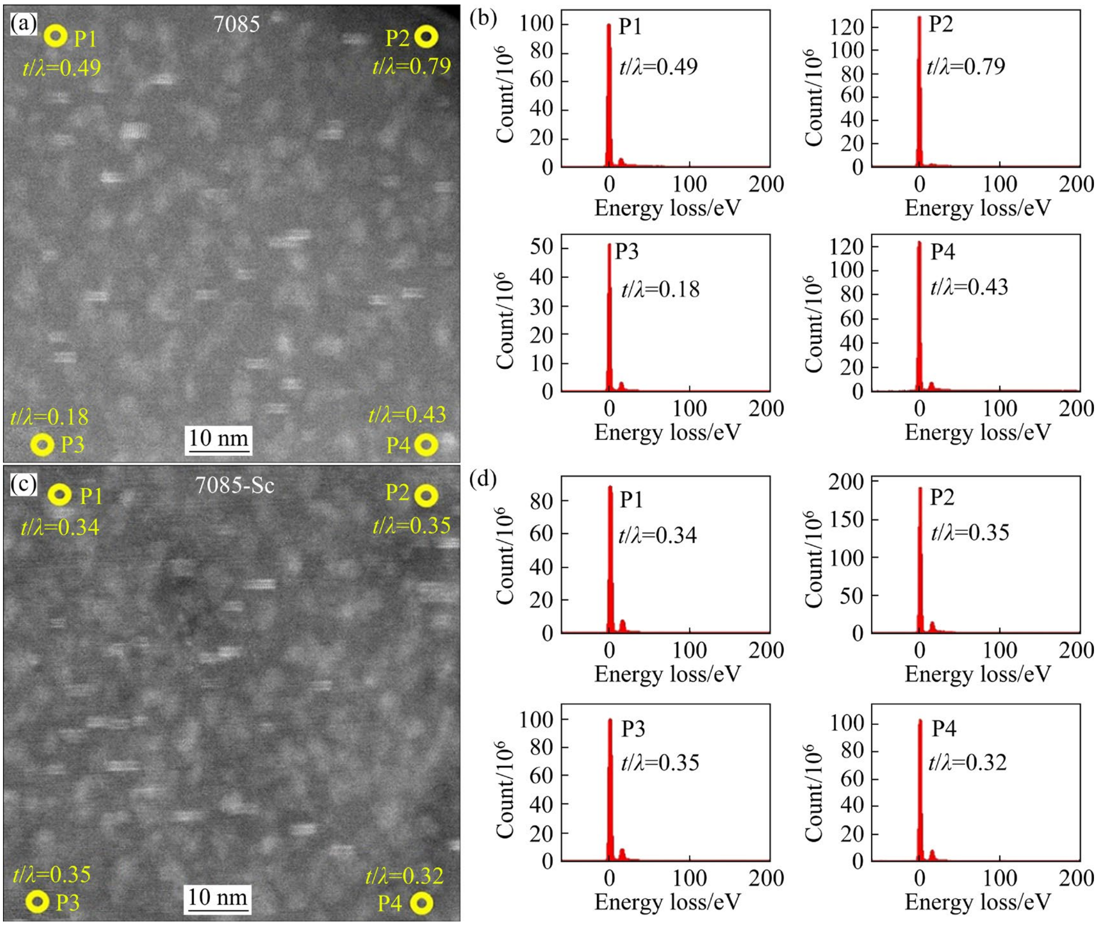

Fig. 13 Number density measurement of GP−η_{p} and η_{p} precipitates in peak-aged 7085 and 7085-Sc alloys revealed by STEM−EELS: (a, b) $[112]_{\text{Al}}$-oriented HAADF image of 7085 alloy and thickness measurement of observing area by zero-loss peaks of EELS acquired from yellow hollow circle positions of P1, P2, P3 and P4 in (a); (c, d) $[112]_{\text{Al}}$-oriented HAADF image of 7085-Sc alloy and thickness measurement of observing area by zero-loss peaks of EELS acquired from yellow hollow circle positions of P1, P2, P3 and P4 in (c)

100 mrad and a probe convergence angle of 18 mrad [51,52]. As a consequence, the peak-aged 7085 alloy has a number density of the precipitates of 1.74×10^{14} mm^{-3} by calculation.

Similarly, Fig. 13(d) shows the relative thickness (t/λ) of the peak-aged 7085-Sc sample at the positions P1, P2, P3 and P4 in Fig. 13(c). The statistical result indicates that the peak-aged 7085-Sc alloy has a number density of the precipitates of 2.14×10^{14} mm^{-3}. Therefore, Sc addition to 7085 alloy induces a higher density of precipitates, which is in line with previous observation [29]. It is expected that Sc addition promotes the nucleation and suppresses the coarsening of GP−η_{p} and η_{p} precipitates in the 7085-Sc alloy during isothermal aging. The solute atoms may combine with vacancies to form solute−vacancy and solute−solute−vacancy complexes. Interaction between solute atoms Sc and vacancies can assist in the formation of Mg−Zn solute clusters and precipitates through the diffusion kinetics process [53]. On the other hand, the Sc−vacancies combination depresses the movement of solute Zn, Mg and Cu, thus effectively inhibiting the coarsening of GP−η_{p} and η_{p} precipitates. Generally, Sc promoted nucleation and Sc suppressed coarsening of the GP−η_{p} and η_{p} precipitates contribute to the higher number density of GP−η_{p} and η_{p} precipitates in the 7085-Sc alloy.

In order to demonstrate Sc involved evolution of the GP−η_{p} and η_{p}, EDS elemental mappings (Fig. 14) at atomic scale were conducted on these two different precipitates in the peak-aged 7085-Sc alloys. Figure 14(a) shows that the observed precipitate belongs to the GP−η_{p}. As expected, the GP−η_{p} mainly contains Zn and Mg (Figs. 14(b, c)).

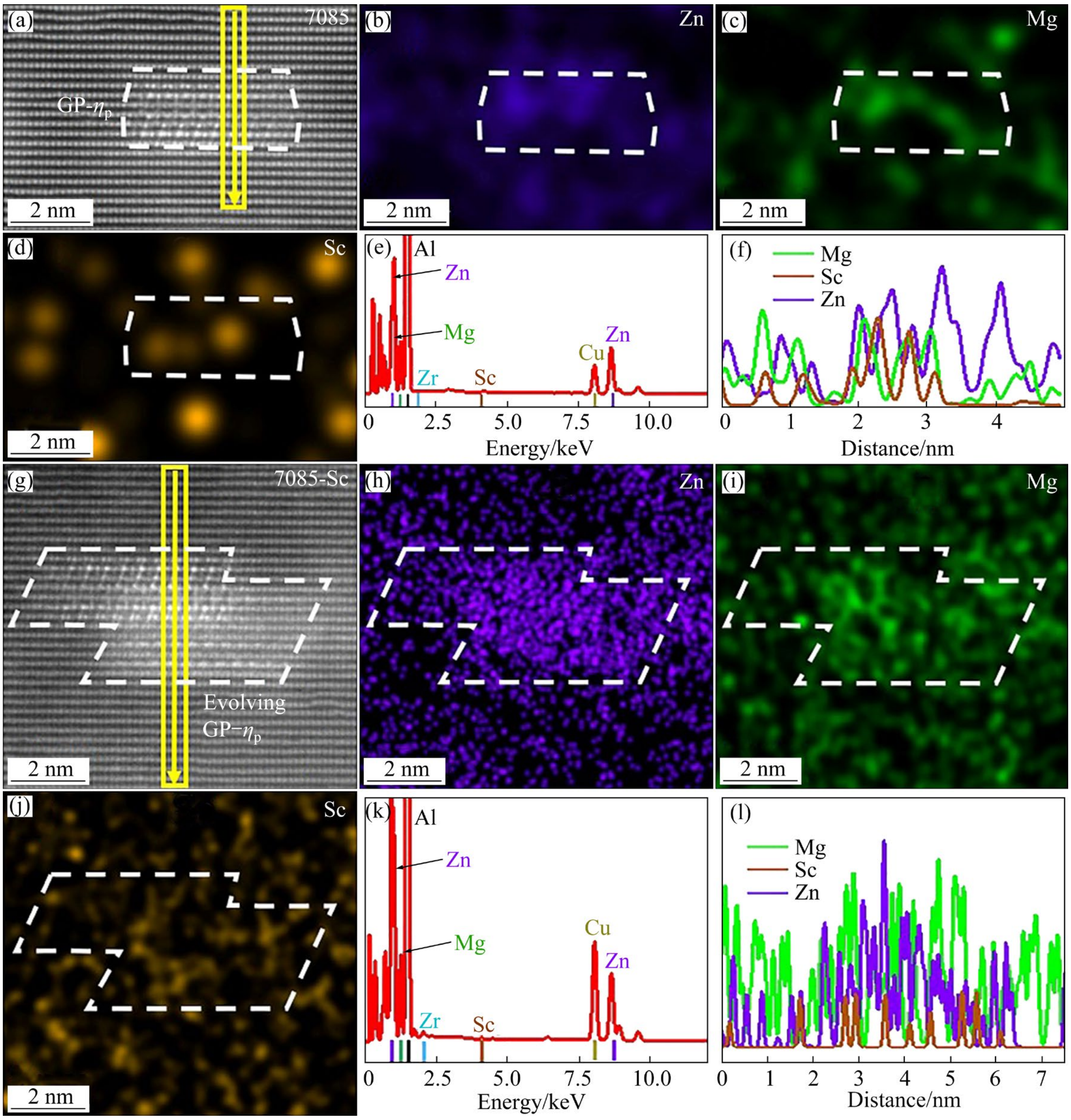

Fig. 14 EDS analyses of GP−η_p in peak-aged 7085 and 7085-Sc alloys: (a−f) Atomic-scale HAADF image of GP−η_p in 7085 alloy, corresponding EDS mappings of Zn, Mg and Sc, EDS spectrum as well as intensity line profiles of Zn, Mg and Sc from yellow rectangle area in (a), respectively; (g−l) Atomic-scale HAADF image of evolving GP−η_p in 7085-Sc alloy, corresponding EDS mappings of Zn, Mg and Sc, EDS spectrum as well as intensity line profiles of Zn, Mg and Sc from yellow rectangle area in (g), respectively

However, minor doping of Sc is also found in the precipitate from the EDS mapping of Sc in Fig. 14(d), which indicates Sc occupation in the GP−η_p. The enrichment of Zn and Mg and minor doping of Sc are also confirmed by the EDS spectrum and line scanning analysis shown in Figs. 14(e, f), respectively. Figure 14(g) shows the atomic-resolution HAADF image of an evolving precipitate from GP−η_p to η_p. Corresponding EDS mapping analysis shows that the evolving GP−η_p also contains Zn and Mg, as shown in Figs. 14(h, i). It is noted that element Sc can also be identified in such precipitate, as shown in Fig. 14(j). The EDS spectrum and line scanning analysis also demonstrate the doping of Sc in evolving GP−η_p, as shown in Figs. 14(k, l). It is reasonable to deduce that the more stable η_p precipitates also have Sc doping during evolution.

It can be concluded that Sc spontaneously dopes into the η_p and GP−η_p precipitates during artificial aging. It is expected that the Sc doping is accompanied by the nucleation and evolution of η_p-series precipitates. It is the doping of Sc to the η_p

and GP−η_p that induces the refinement, increases number density and suppresses GP−η_p/η_p transition of the peak-aging precipitates in the 7085-Sc alloy relative to the 7085 alloy. Predictably, the interaction between Sc and peak-aging precipitates will also persist into the over-aging stage, eventually resulting in a retarded formation of η precipitates with less strengthening effect during over-aging treatment. This explains higher hardness value of 7085-Sc alloy than that of 7085 alloy in the over-aging stage. The detailed determination of precipitate microstructure in the over-aging stage is also particular important and will be a further direction of research.

3.5 Δ*H* of modified GP−η_p and η_p with some atoms substituted by Sc

To better validate the rationality of the Sc-doped GP−η_p and η_p detected by STEM−EDS, the first-principles formation enthalpies (Δ*H*) were calculated for different structures with part of atoms in the precipitates substituted by Sc, as shown in Fig. 15. The formation enthalpy represents a driving force for a more stable phase transformation, and a lower formation enthalpy indicates an easier phase formation among identical precipitate structures. Figures 15(a, b) show that the perfect GP−η_p and η_p without any Sc substitution have formation enthalpies of around −2.5 kJ/mol per atom and −7.5 kJ/mol per atom, respectively, suggesting these two precipitates are stable in energy. Similar Δ*H* values of GP−η_p and η_p were also obtained in a previous study [18]. The change in Δ*H* as a function of various substitution amounts of Al by Sc (denoted as xAl$_{\mathrm{Sc}}$) in GP−η_p reveals a gradual decrease in Δ*H* from unsubstituted structure (GP−η_p-0Al$_{\mathrm{Sc}}$) at −2.5 kJ/mol per atom to GP−η_p with 17% Al substituted by Sc (GP−η_p-0.17Al$_{\mathrm{Sc}}$) at −12 kJ/mol per atom. There is a nearly unchanged Δ*H* for GP−η_p-(0.17−0.28)Al$_{\mathrm{Sc}}$ and a consecutively increased Δ*H* for GP−η_p-(0.28−1.00)Al$_{\mathrm{Sc}}$. This strongly suggests that the internal Al atoms of GP−η_p can be partially substituted with Sc due to the decreased Δ*H*, being consistent with our experimental observations of Figs. 14(a−f).

Figure 15(b) compares the calculated Δ*H* of the structures with different amounts of Zn, Mg and Al in the η_p substituted by Sc. Clearly, both substitutions of Mg and Al by Sc are energetically favorable due to the decreased Δ*H* of η_p-Mg$_{\mathrm{Sc}}$ and η_p-Al$_{\mathrm{Sc}}$, which signifies that the substitutions of Mg and Al in η_p by Sc are feasible in the practical process. In comparison, there is a slightly decreased Δ*H* of η_p with 12% Zn substituted by Sc (namely η_p-0.12Zn$_{\mathrm{Sc}}$) relative to the perfect η_p. The further substitution results in a consecutive increase in Δ*H* for the η_p-(0.12−1.0)Zn$_{\mathrm{Sc}}$ structures. This implies that a small amount of Zn$_{\mathrm{Sc}}$ could occur in the η_p precipitate. In general, partial Mg, Al and Zn in η_p can be substituted by solute Sc during thermal aging treatment, which is in line with the STEM−EDS result of Fig.14(l). The observed Sc-doped η_p and GP−η_p further substantiate the refined size and increase number density of precipitates shown in Figs. 11 and 13 since the doped Sc could well imped the growth and coarsening of the precipitates [49]. It is the Sc doping that results in an increased proportion of GP−η_p in the Sc-containing 7085 alloy shown in Fig. 12.

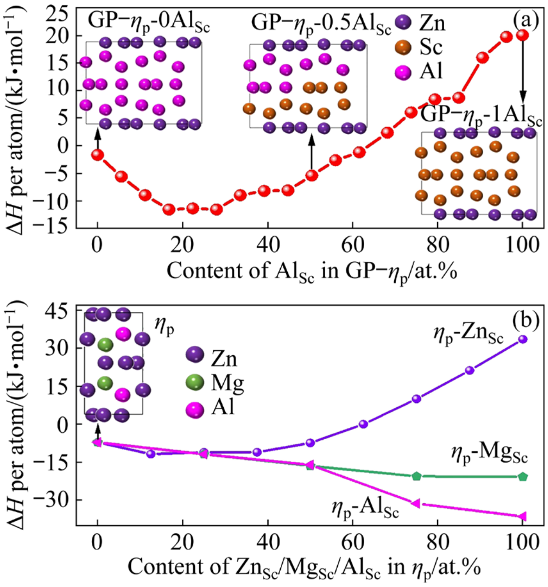

Fig. 15 First-principles formation enthalpies of GP−η_p, η_p and their modified structures with different contents of A atoms replaced with Sc (denoted as xA$_{\mathrm{Sc}}$): (a) Δ*H* change of GP−η_p with internal Al atoms replaced with different contents of Sc; (b) Δ*H* change of η_p with Zn, Mg and Al replaced with different contents of Sc (A=Al, Mg, Zn)

Basically, the present experimental results suggest that the Al grain refinement contributes to a strength increase of 12 MPa and the precipitate change increases the strength of around 5 MPa due to Sc addition to 7085 alloy. The possible reasons are as follows. First, statistical result shows that Sc minor addition to 7085 alloy leads to a slight size refinement (Fig. 11) and number density increase

(Fig. 13) of the disc-like precipitates. Thus, the contribution of the precipitate refinement to the strength increase is limited. Second, the result of Fig. 8 indicates that $\text{Al}_3\text{Sc@Al}_3\text{(Sc,Zr)}$ has a larger interfacial Al strain field than Al_3Zr precipitates, which probably contributes to the partial strength increase of 7085-Sc alloy. Furthermore, additional research is needed to explore the differences in strengthening effect between GP−η_p and η_p precipitates though the peak-aged 7085-Sc alloy has a larger fraction of GP−η_p than the peak-aged 7085 alloy. Therefore, the current study concludes that the increased yield strength of the peak-aged 7085-Sc alloy relative to the 7085 alloy is mainly resulted from the Sc-induced Al grain refinement.

3.6 Grain boundary precipitates (GBPs) and precipitation free zones

Figures 16(a, b) show that the size of grain boundary precipitates (GBPs) in two peak-aged alloys is universally larger than that of the precipitates inside Al grains. The high energy grain boundary always serves as the preferential site for phase nucleation and coarsening during heat treatment [54]. It is observed that there is a discontinuous distribution of these GBPs on grain boundaries. The measurement shows that the GBPs in the 7085 alloy have an average size of ~25 nm, whereas smaller GBPs (~10 nm in size) are identified in the 7085-Sc alloy. The STEM−EDS elemental mapping analysis shows that the GBPs in the peak-aged 7085 alloy are rich in Zn, Mg and Cu (Figs. 16(c−h)), which belong to η particles containing Cu [55]. However, the GBPs in the peak-aged 7085-Sc alloy are observed to have Sc doping in addition to Zn, Mg and Cu (Figs. 16(i−n)). Consequently, the Sc doping contributes to a pronounced refining effect of the GBPs, which agrees with the case of the second-phase particles at the grain boundary presented in Figs. 5(b, d). Figures 16(o, p) compare the width of precipitation free zones (PFZ) in the peak-aged 7085 and 7085-Sc alloys, respectively. The red dashed rectangle areas in Figs. 16(o, p)) were enlarged to see more details about the PFZ, as shown in their corresponding insets. The measurement results show a PFZ width of ~28.5 nm for 7085 alloy and an evidently decreased FPZ width of ~20.3 nm for 7085-Sc alloy.

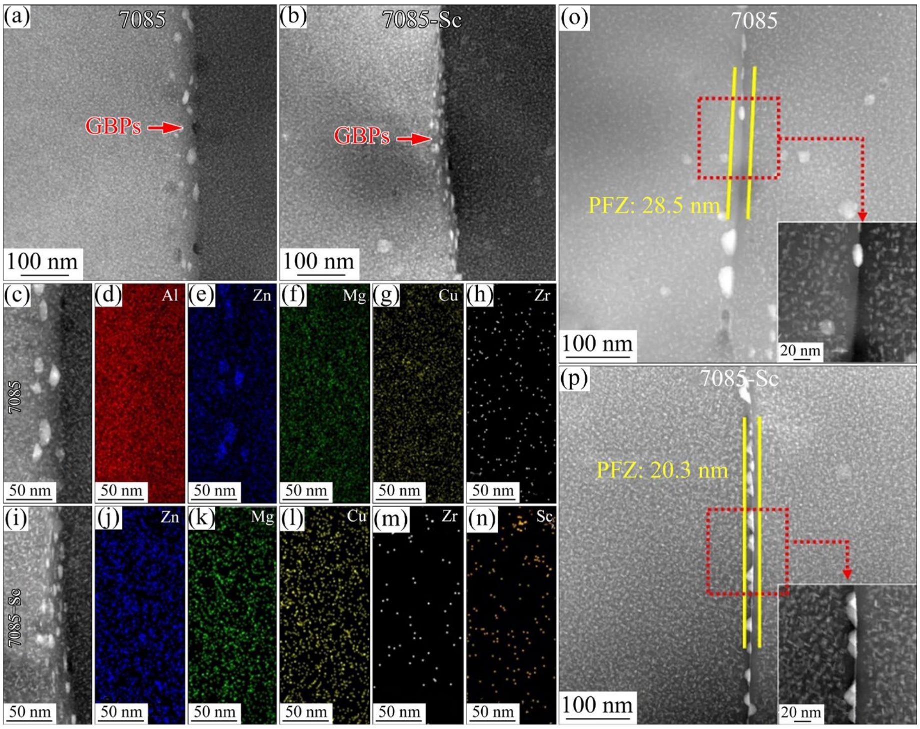

Fig. 16 HAADF images and EDS mapping analyses showing GBPs and PFZ of peak-aged 7085 and 7085-Sc samples: (a, b) HAADF images displaying configuration of GBPs in 7085 and 7085-Sc alloys, respectively; (c−h, i−n) HAADF images and corresponding EDS mappings of GBPs in 7085 and 7085-Sc alloys, respectively; (o, p) HAADF images and corresponding enlargement of red dashed rectangle areas (insets) providing PFZ width in 7085 and 7085-Sc alloys, respectively

In the 7085-Sc alloy illustrated in Fig. 16(p), the significantly reduced PFZ width is caused by the Sc-containing grain boundaries (Fig. 16(n)).

The difference of IGC of the 7085 and 7085-Sc alloys is explained as follows. The preferential dissolution of Mg occurs when the larger GBPs enriched in Mg, Zn and Cu are in contact with the corrosive solution because Mg is more anodic than Al, Zn, and Cu [56]. Then, the Zn with less passivation than Al begins to dissolve and residual Cu-enriched GBPs are formed. Subsequently, more anodic Cu-depletion PFZ adjacent to the Cu-enriched GBPs starts to dissolve since Cu is more noble than Al, thereby leading to the onset of IGC. The more Cu-depleted matrix near the PFZ than the matrix far away from the GBs should also undergo dissolution, albeit with less preference compared to the PFZs, due to the fact that solute elements in Cu-depleted matrix diffuse not only into the GBPs but also into the matrix precipitates [57]. The larger the particle size of the GBPs, the larger the contact area with the matrix. When the large GBPs partially dissolve in contact with the corrosive solution, the Al matrix near the Cu rich region begins to corrode, increasing the rate of intergranular corrosion. It is accepted that EFC belongs to a type of IGC and produces a larger volume than the original aluminum alloy [58]. The resulted expansion-induced stresses lift the surface grains and then expose the underlying material.

4 Conclusions

(1) Compared to 7085 alloy, the hardness and tensile strength of 7085-Sc alloy were increased by ~HV 8 and ~17 MPa, respectively, at peak aging state, along with the unchanged age-hardening response. The increase in the strength of 7085-Sc alloy is mainly attributed to the refined Al grains, strong interfacial Al strain field induced by Al_3Sc@$Al_3(Sc,Zr)$ nanoparticles and high-density GP−η_p and η_p containing Sc. The Sc doping in GP−η_p and η_p precipitates suppresses phase transformation from GP−η_p to η_p.

(2) First-principles calculations indicate that Zr has stronger electron transfer than Sc to neighboring Al atoms at the $Al_3(Sc,Zr)$/Al interface, forming ionic bonding at the interface in addition to metallic bond. In contrast to the Al_3Zr/Al, there is a decreased DOS (corresponding to the electrical conductivity) for the most energetically favored $Al_3(Sc_{0.2},Zr_{0.8})$/Al configuration.

(3) Sc addition to 7085 alloy results in the modification of IGC and EFC due to the decreased Al grain size, PFZ width and Sc-doped GBPs of η phases with promoted potential.

CRediT authorship contribution statement

Ting-bin LIANG: Methodology, Investigation, Formal analysis, Writing − Original draft, Data curation; **Hong WANG:** Investigation, Formal analysis, Data curation; **Jia-hai LI:** Investigation, Formal analysis; **Zhi-chao YANG:** Investigation, Formal analysis; **Bin WANG:** Investigation, Formal analysis; **De-yu ZHANG:** Investigation, Formal analysis; **Xiang-yi ZHANG:** Investigation, Formal analysis; **Asad ALI:** Writing − Review & editing; **Xi-zhou KAI:** Investigation, Formal analysis; **Yu-tao ZHAO:** Investigation, Formal analysis, **Shuang-bao WANG:** Conceptualization, Funding acquisition, Supervision, Project administration, Writing − Review & editing.

Declaration of competing interest

The authors declare that they have no known competing financial interests or personal relationships that could have appeared to influence the work reported in this paper.

Data availability statement

The data supporting the findings of this study are available from the corresponding author on request.

Acknowledgments

The authors appreciate the support from the National Natural Science Foundation of China (Nos. U20A20274, 52061003), the Natural Science Foundation of Yunnan Province, China (No. 202301AT070209) and the Science and Technology Major Project of Yunnan Province, China (No. 202102AG050017).

References

[1] FRIDLYANDER I N, SENATOROVA O G. Development and application of high-strength Al−Zn−Mg−Cu alloys [J]. Materials Science Forum, 1996, 217−222: 1813−1818.

[2] ANDERSEN S J, MARIOARA C D, FRIIS J, WENNER S, HOLMESTAD R. Precipitates in aluminium alloys [J]. Advances in Physics: X, 2018, 3: 1479984.

[3] OU Yi-zi, JIANG Yong, WANG Yi-ren, LIU Zheng-qing, LERVIK A, HOLMESTAD R. Vacancy and solute co-segregated η1 interface in over-aged Al−Zn−Mg alloys [J].

Acta Materialia, 2021, 218: 117082.

[4] ZHAO Huan, CHAKRABORTY P, PONGE D, HICKEL T, SUN Bin-han, WU Chun-hung, GAULT B, RAABE D. Hydrogen trapping and embrittlement in high-strength Al alloys [J]. Nature, 2022, 602: 437−441.

[5] YING Tao, GU Li-dong, TANG Xiao-yi, WANG Jing-ya, ZENG Xiao-qin. Effect of Sc microalloying on microstructure evolution and mechanical properties of extruded Al−Zn−Mg−Cu alloys [J]. Materials Science and Engineering A, 2022, 831: 142197.

[6] CLOUET E, LAE L, EPICIER T, LEFEBVRE W, NASTAR M, DESCHAMPS A. Complex precipitation pathways in multicomponent alloys [J]. Nature Materials, 2006, 5: 482−488.

[7] PAN Shuai, CHEN Xin-jian, LIAO Gui-zhen, ALI A, WANG Shuang-bao. Developing a high-performance Al−Mg−Si−Sn−Sc alloy for essential room-temperature storage after quenching: Aging regime design and micromechanisms [J]. Rare Metals, 2023, 42: 3814−3828.

[8] ZHANG Xing-pu, HAN Zhong-kang, XU Liang-liang, NI Hao-han, HU Xiao-juan, ZHOU Hao-fei, ZOU Yu, WANG Jiang-wei. Evolution of precipitate and precipitate/matrix interface in Al−Zn−Mg−Cu(−Ag) alloys [J]. Journal of Materials Science & Technology, 2023, 138: 157−170.

[9] PENG Ying-hao, LIU Chong-yu, WEI Li-li, JIANG Hong-jie, GE Zhen-jiang. Quench sensitivity and microstructures of high-Zn-content Al−Zn−Mg−Cu alloys with different Cu contents and Sc addition [J]. Transactions of Nonferrous Metals Society of China, 2021, 31: 24−35.

[10] MUKHERJEE D, ROY H, CHANDRAKANTH B, MANDAL N, SAMANTA S K, MUKHERJEE M. Enhancing properties of Al−Zn−Mg−Cu alloy through microalloying and heat treatment [J]. Materials Chemistry and Physics, 2024, 314: 128881.

[11] HUANG Xing, PAN Qing-lin, LI Bo, LIU Zhi-ming, HUANG Zhi-qi, YIN Zhi-min. Microstructure, mechanical properties and stress corrosion cracking of Al−Zn−Mg−Zr alloy sheet with trace amount of Sc [J]. Journal of Alloys and Compounds, 2015, 650: 805−820.

[12] KUPTSOV S G, ELANTSEV A V, NIKONENKO E A. Effect of heterogenizing annealing on the structure and the hardness of a high-strength 01979 aluminum alloy produced by granular technology from the melt [J]. Russian Metallurgy (Metally), 2015, 2015: 606−610.

[13] HUA Lin, HU Xuan, HAN Xing-hui. Microstructure evolution of annealed 7075 aluminum alloy and its influence on room-temperature plasticity [J]. Materials & Design, 2020, 196: 109192.

[14] FRIAUF J B. The crystal structure of magnesium di-zincide [J]. Physical Review, 1927, 29: 34−40.

[15] LI Zhen-liang, XIE Jian-xin, CHEN Wei, ZHAI Jing, REN Hui-ping, WANG Yu-feng. Structure and property of nickel-modified ultrahigh strength Al−Zn−Mg−Cu alloy by spray forming [J]. Materials Science Forum, 2007, 546/547/548/549: 871−876.

[16] LIU Ji-zi, CHEN Jiang-hua, YUAN Ding-wang, WU Cui-lan, ZHU Jing, CHENG Zhi-ying. Fine precipitation scenarios of AlZnMg(Cu) alloys revealed by advanced atomic-resolution electron microscopy study. Part I: Structure determination of the precipitates in AlZnMg(Cu) alloys [J]. Materials Characterization, 2015, 99: 277−286.

[17] LIU Chun-hui, FENG Zhuang-zhuang, MA Pei-pei, ZHOU Yi-hui, LI Guo-hui, ZHAN Li-hua. Reversion of natural ageing and restoration of quick bake-hardening response in Al−Zn−Mg−Cu alloy [J]. Journal of Materials Science & Technology, 2021, 95: 88−94.

[18] LIU Ji-zi, CHEN Jiang-hua, LIU Zi-ran, WU Cui-lan. Fine precipitation scenarios of AlZnMg(Cu) alloys revealed by advanced atomic-resolution electron microscopy study. Part II: Fine precipitation scenarios in AlZnMg(Cu) alloys [J]. Materials Characterization, 2015, 99: 142−149.

[19] TANG Jie, LIU Ming-cai, BO Guo-wei, JIANG Fu-lin, LUO Chun-hui, TENG Jie, FU Ding-fa, ZHANG Hui. Unraveling precipitation evolution and strengthening function of the Al−Zn−Mg−Cu alloys with various Zn contents: Multiple experiments and integrated internal-state-variable modeling [J]. Journal of Materials Science & Technology, 2022, 116: 130−150.

[20] MA Yu, AHMED A, JI Gang, ZHANG Ming-xing, LEFEBVRE W, CHEN Zhe, JI V. Atomic-scale investigation of the interface precipitation in a TiB_2 nanoparticles reinforced Al−Zn−Mg−Cu matrix composite [J]. Acta Materialia, 2020, 185: 287−299.

[21] LI X Z, HANSEN V, GJØNNES J, WALLENBERG L R. HREM study and structure modeling of the η' phase, the hardening precipitates in commercial Al−Zn−Mg alloys [J]. Acta Materialia, 1999, 47: 2651−2659.

[22] WOLVERTON C. Crystal structure and stability of complex precipitate phases in Al−Cu−Mg−(Si) and Al−Zn−Mg alloys [J]. Acta Materialia, 2001, 49: 3129−3142.

[23] CHUNG T F, YANG Yo-lun, HUANG Bo-ming, SHI Zhu-sheng, LIN Jian-guo, OHMURA T, YANG J R. Transmission electron microscopy investigation of separated nucleation and in-situ nucleation in AA7050 aluminium alloy [J]. Acta Materialia, 2018, 149: 377−387.

[24] ROYSET J. Scandium in aluminium alloys: Physical metallurgy, properties and applications [J]. Metallurgical Science and Tecnology, 2007, 25: 11−21.

[25] RØYSET J, RYUM N. Scandium in aluminium alloys [J]. International Materials Reviews, 2005, 50: 19−44.

[26] ZHANG Miao, LIU Tao, HE Chun-nian, DING Jian, LIU En-zuo, SHI Chun-sheng, LI Jia-jun, ZHAO Nai-qin. Evolution of microstructure and properties of Al−Zn−Mg−Cu−Sc−Zr alloy during aging treatment [J]. Journal of Alloys and Compounds, 2016, 658: 946−951.

[27] YE Ji, PAN Qing-lin, LIU Bing, HU Quan, QU Long-feng, WANG Wei-yi, WANG Xiang-dong. Effects of co-addition of minor Sc and Zr on aging precipitates and mechanical properties of Al−Zn−Mg−Cu alloys [J]. Journal of Materials Research and Technology, 2023, 22: 2944−2954.

[28] XIAO Quan-feng, HUANG Ji-wu, JIANG Ying-ge, JIANG Fu-qin, WU Yun-feng, XU Guo-fu. Effects of minor Sc and Zr additions on mechanical properties and microstructure evolution of Al−Zn−Mg−Cu alloys [J]. Transactions of Nonferrous Metals Society of China, 2020, 30: 1429−1438.

[29] LIU Jing, YAO Pei, ZHAO Nai-qin, SHI Chun-sheng, LI Hui-

jun, LI Xuan, XI De-sheng, YANG Shuo. Effect of minor Sc and Zr on recrystallization behavior and mechanical properties of novel Al−Zn−Mg−Cu alloys [J]. Journal of Alloys and Compounds, 2016, 657: 717−725.

[30] XU Ai-jun, HAN Jia-qiang, WANG Hui-min, ZHENG Wen-yue, NIU Kang-min. Progress in dispersoids distribution precipitating during homogenising Zr-containing Al−Cu−Li and Al−Zn−Mg alloys [J]. Materials Science and Technology, 2020, 36: 1903−1921.

[31] KNIPLING K E, KARNESKY R A, LEE C P, DUNAND D C, SEIDMAN D N. Precipitation evolution in Al−0.1Sc, Al−0.1Zr and Al−0.1Sc−0.1Zr (at.%) alloys during isochronal aging [J]. Acta Materialia, 2010, 58: 5184−5195.

[32] MARQUIS E A, SEIDMAN D N. Nanoscale structural evolution of Al_3Sc precipitates in Al(Sc) alloys [J]. Acta Materialia, 2001, 49: 1909−1919.

[33] FULLER C B, SEIDMAN D N, DUNAND D C. Mechanical properties of Al(Sc,Zr) alloys at ambient and elevated temperatures [J]. Acta Materialia, 2003, 51: 4803−4814.

[34] ZHANG Yong, WEYLAND M, MILKEREIT B, REICH M, ROMETSCH P A. Precipitation of a new platelet phase during the quenching of an Al−Zn−Mg−Cu alloy [J]. Scientific Reports, 2016, 6: 23109.

[35] SUN Yu-qiao, LUO Yu-hong, PAN Qing-lin, LIU Bing, LONG Liang, WANG Wei-yi, YE Ji, HUANG Zhi-qi, XIANG Sheng-qian. Effect of Sc content on microstructure and properties of Al−Zn−Mg−Cu−Zr alloy [J]. Materials Today Communications, 2021, 26: 101899.

[36] TENG G B, LIU C Y, MA Z Y, ZHOU W B, WEI L L, CHEN Y, LI J, MO Y F. Effects of minor Sc addition on the microstructure and mechanical properties of 7055 Al alloy during aging [J]. Materials Science and Engineering A, 2018, 713: 61−66.

[37] ASTM G110 — 92. Standard practice for evaluating intergranular corrosion resistance of heat treatable aluminum alloys by immersion in sodium chloride + hydrogen peroxide solution [S]. 2015.

[38] NELLIST P D, PENNYCOOK S J. Incoherent imaging using dynamically scattered coherent electrons [J]. Ultramicroscopy, 1999, 78: 111−124.

[39] CLARK S J, SEGALL M D, PICKARD C J, HASNIP P J, PROBERT M I J, REFSON K, PAYNE M C. First principles methods using CASTEP [J]. Zeitschrift fuer Kristallographie, 2005, 220: 567−570.

[40] WOLVERTON C, OZOLIŅŠ V. First-principles aluminum database: Energetics of binary Al alloys and compounds [J]. Physical Review B, 2006, 73: 144104.

[41] WEI Bo, PAN Shuai, LIAO Gui-zhen, ALI Asad, WANG Shuang-bao. Sc-containing hierarchical phase structures to improve the mechanical and corrosion resistant properties of Al−Mg−Si alloy [J]. Materials & Design, 2022, 218: 110699.

[42] LIAO Gui-zhen, WEI Bo, PAN Shuai, WANG Shuang-bao. Phase structure modification-based property improvement of Al−4.3Cu−1.6Mg−0.2Sc (wt.%) alloy [J]. Materials Characterization, 2023, 196: 112664.

[43] SHI Yun-jia, PAN Qing-lin, LI Meng-jia, HUANG Xing, LI Bo. Effect of Sc and Zr additions on corrosion behaviour of Al−Zn−Mg−Cu alloys [J]. Journal of Alloys and Compounds, 2014, 612: 42−50.

[44] JAMES T B, SANGSHIK K, RICHARD P G. Effect of corrosion severity on fatigue evolution in Al−Zn−Mg−Cu [J]. Corrosion Science, 2010, 52: 498−508.

[45] IWAMURA S, MIURA Y. Loss in coherency and coarsening behavior of Al_3Sc precipitates [J]. Acta Materialia, 2004, 52: 591−600.

[46] LEFEBVRE W, DANOIX F, HALLEM H, FORBORD B, BOSTEL A, MARTHINSEN K. Precipitation kinetic of Al_3(Sc,Zr) dispersoids in aluminium [J]. Journal of Alloys and Compounds, 2009, 470: 107−110.

[47] KHARAKTEROVA M L, ESKIN D G, TOROPOVA L S. Precipitation hardening in ternary alloys of the Al□Sc□Cu and Al□Sc□Si systems [J]. Acta Metallurgica et Materialia, 1994, 42: 2285−2290.

[48] WANG Shuang-bao, LIU Yu-ying, LIU Yun, SHI Zhi-hao, ZHOU Jian, ZHU Jia-jun, HU Wan-biao. Identifying the surface properties of $Ti_3C_2T_x$ MXene through transmission electron microscopy [J]. Cell Reports Physical Science, 2022, 3: 101151.

[49] XUE Hang, YANG Chong, DE G F, ZHANG Peng, ZHANG Jin-yu, CHEN Bin, LIU Fu-zhu, PENG Yong, BIAN Jian-jun, LIU Gang, DESCHAMPS A, SUN Jun. Highly stable coherent nanoprecipitates via diffusion-dominated solute uptake and interstitial ordering [J]. Nature Materials, 2022, 22: 434−441.

[50] KWON E P, WOO K D, KIM S H, KANG D S, LEE K J, JEON J Y. The effect of an addition of Sc and Zr on the precipitation behavior of AA6061 alloy [J]. Metals and Materials International, 2010, 16: 701−707.

[51] MALIS T, CHENG S C, EGERTON R F. EELS log-ratio technique for specimen-thickness measurement in the TEM [J]. Journal of Electron Microscopy Technique, 1988, 8: 193−200.

[52] WANG Shuang-bao, PAN Cheng-fu, WEI Bo, ZHENG Xiong, LAI Yu-xiang, CHEN Jiang-hua. Nano-phase transformation of composite precipitates in multicomponent Al−Mg−Si(−Sc) alloys [J]. Journal of Materials Science & Technology, 2022, 110: 216−226.

[53] ZHANG Xing-pu, XU Liang-liang, HU Wen-xin, ZHOU Hao-fei, WANG Jiang-wei. Effects of Sc on the vacancy and solute behaviours in aluminium [J]. Journal of Materials Science & Technology, 2023, 148: 41−51.

[54] SHENG X Y, SHANG Z, SHANG A Y, WANG H, ZHANG X. Grain boundary and twin boundary solute segregations in nanocrystalline Al−Mg alloy [J]. Scripta Materialia, 2024, 245: 116053.

[55] CAO Pu-li, LI Cheng-bo, ZHU Dai-bo, ZHAO Cai, XIAO Bo, ZHANG Xin-Ming. Heterogeneous precipitation behavior of 7085 aluminum alloy was studied by high-throughput experiment based on end-quenching technology [J]. Metals and Materials International, 2024, 30: 1965−1976.

[56] JONES D A. Principles and prevention of corrosion [M]. New York: Macmillan Publishing Company, 1996.

[57] XIONG Yi-da, ROBSON J D, CAO Zhen-jie, DENG Yang-chao, YAO Yi-chao, ZHONG Xiang-li, BENDO A, LV Jin-long, GUARRACINO F, DONOGHUE J, CURIONI M. Mitigation effects of over-aging (T73) induced intergranular

corrosion on stress corrosion cracking of AA7075 aluminum alloy and behaviors of η phase grain boundary precipitates during the intergranular corrosion formation [J]. Corrosion Science, 2023, 225: 111570.

[58] ÖZER G, KARAASLAN A. Effects of RRA heat treatment on the exfoliation corrosion (EXCO), intergranular corrosion (IGC), and electrical conductivity of AA7075 alloy [J]. Materials and Corrosion, 2019, 70: 549−557.

微量 Sc 对 AA7085 合金显微组织和性能的影响

梁庭斌 [1]，王　红 [1]，李加海 [1]，杨智超 [1]，王　斌 [1]，
张德宇 [1]，张翔一 [1]，Asad ALI [2]，怯喜周 [3]，赵玉涛 [3]，王双宝 [1,4]

1. 云南大学 材料与能源学院 云南省电磁材料与器件重点实验室，昆明 650091；
2. Division of Energy Science, Luleå University of Technology, Luleå 97187, Sweden;
3. 江苏大学 材料科学与工程学院，镇江 212013；
4. 云南大学 电镜中心，昆明 650091

摘　要：比较了添加和不添加 0.3%(质量分数)Sc 的 AA7085 合金的时效硬化响应、力学和耐腐蚀性能，并使用球差校正透射电子显微术和第一性原理计算揭示了 Sc 微合金化的微观机制。结果表明，AA7085-Sc 合金强度的增加主要归因于 Al 晶粒尺寸的减小以及 $\mathrm{Al_3Sc@Al_3(Sc,Zr)}$核壳纳米颗粒和含 Sc 的 η_{P}、GP−η_{P} 纳米析出相数量密度的增加。在 $\mathrm{Al_3Sc@Al_3(Sc,Zr)/Al}$ 界面处存在强烈的应变场以及 Zr 与相邻基体 Al 原子之间明显的电子转移。Sc 在 GP−η_{P} 和 η_{P} 中的掺杂抑制 GP−η_{P} 向 η_{P} 的转变。与 7085 合金相比，AA7085-Sc 合金的耐腐蚀性得到改善，这与更细小的 η 相晶界沉淀物和更窄的晶界无析出带有关。基于多尺度的显微组织表征技术，揭示 Sc 微合金化后 AA7085 合金性能变化的原因。

关键词：7085 铝合金；Sc 微合金化；显微组织；性能；透射电子显微术

(Edited by Bing YANG)